

A systematic characterisation of canopy density based on turbulent-structure penetration

Zishen Chen¹ and Ricardo García-Mayoral^{1†}

¹Department of Engineering, University of Cambridge, Trumpington Street, Cambridge CB2 1PZ, UK

(Received xx; revised xx; accepted xx)

Turbulent flows over canopies of rigid elements with different geometries, spacings and Reynolds numbers are investigated to identify and characterise different canopy density regimes. In the sparse regime, turbulence penetrates relatively unhindered within the canopy, whereas in the dense regime, this penetration is limited. A common measure of canopy density is the ratio of frontal area to bed area, the frontal density λ_f . While effective for conventional vegetation canopies with no preferential orientation, we observe that λ_f does not accurately predict the density regime for some less conventional canopy topologies, suggesting that it does not necessarily encapsulate the physics governing the canopy density. To address this, we adopt a direct approach that quantifies the degree of penetration of the overlying turbulence into the canopy. We propose density metrics based on the position and extent of individual flow eddies, in particular those of intense Reynolds shear stress $u'v'$. We use these metrics to analyse a series of direct numerical simulations for both isotropic- and anisotropic-layout canopies across a range of frontal densities $\lambda_f \approx 0.01$ -2.04, heights $h^+ \approx 44$ -266, element width-to-pitch ratios $w/s \approx 0.06$ -0.7, and Reynolds numbers $Re_\tau \approx 180$ -2000. Our results show that canopies with elements closely packed in the streamwise direction but large spanwise gaps allow for significant turbulence penetration, and thus appear sparser compared to isotropic or spanwise-packed canopies with the same λ_f . When the spanwise gap is fixed, turbulence penetration remains similar and largely independent of the streamwise pitch and gap between elements. As the spanwise gap increases, eddies penetrate deeper and more vigorously into the canopy. We also show that canopy density and turbulence penetration are Reynolds-number-dependent. A canopy with a fixed geometry can exhibit a dense-like behaviour at low Re_τ , but enhanced turbulent penetration as Re_τ increases. Our results suggest that the penetration of overlying eddies depends essentially on the spanwise gap between canopy elements and its relative size compared to the typical width of the overlying eddies. Turbulence penetrates easily into the canopy when the spanwise gap is larger than the eddy size, and is essentially precluded from penetrating in the opposite case. A penetration length can then be defined that is of the order of the spanwise gap or the eddy size, whichever is smaller. If the penetration length is small compared to the canopy height, the canopy behaves as dense; if it is comparable, the canopy has an intermediate behaviour; and if it is approximately equal or larger than the canopy height, the eddies penetrate all the way to the canopy bed and the canopy behaves as sparse.

Key words: turbulent boundary layers

† Email address for correspondence: r.gmayoral@eng.cam.ac.uk

1. Introduction and background

Canopies of protruding elements are ubiquitous in practical flows, holding significant environmental and engineering importance. Vegetation canopies are of great ecological importance to both terrestrial and aquatic ecosystems, mediating the concentration of nutrients, oxygen, and carbon (Malhi 2002; Baldocchi 2003), as reviewed by Finnigan (2000), Belcher *et al.* (2012), Nepf (2012*a,b*) and Brunet (2020). Canopies of pin-fin arrays are widely used in industrial applications for heat transfer enhancement (Ligrani *et al.* 2003; Peles *et al.* 2005; Arshad *et al.* 2017), as summarised in Mousa *et al.* (2021). The study of canopy turbulence is also relevant to a wide range of applications, including cooling urban heat islands (Akbari & Kolokotsa 2016; Rahman *et al.* 2020), mitigating agricultural loss due to windthrow (Berry *et al.* 2004; De Langre 2008), monitoring the transport of airborne pollutants (Belcher 2005; Escobedo *et al.* 2011; Janhäll 2015), and forecasting weather (Britter & Hanna 2003; Blocken 2015). Consequently, understanding the interaction between canopies and turbulence is crucial for effectively managing such practical flows and improving the related environmental and industrial practice.

Canopy density has a direct impact on the turbulent flow within and immediately above the canopy (Nepf 2012*a*; Brunet 2020; Sharma & García-Mayoral 2020*a,b*). Poggi *et al.* (2004) conducted experiments on flows over various canopy densities and identified the characteristics of different density regimes, suggesting that the flow over canopies can be broadly divided into three components. A graphical illustration of these components and their characteristic eddies for dense and sparse canopies is depicted in figure 1. The first component is the background turbulence characteristic of boundary layers – this is the component that would be present even in the absence of the canopy. The second component is the element-induced or element-coherent flow, which mainly occurs within the canopy and results from the obstruction caused by individual elements (Cava & Katul 2008; Dupont *et al.* 2011). The third component is the mixing-layer-like flow that forms due to the mean-flow inflection in the vicinity of the canopy-tip plane of a dense canopy (Raupach *et al.* 1996; Finnigan 2000). Poggi *et al.* (2004) emphasised that the flow behaviour near the canopy-tip plane is largely dependent on the canopy density regime, and that mixing-layer-like eddies only appear when the canopy density is high enough to induce a strong and relatively homogeneous shear layer (Raupach *et al.* 1996; Sharma & García-Mayoral 2020*b*). If we consider the eddies from the background turbulence as they penetrate into the canopy, their relative intensity and penetration depth vary depending on the canopy density (Nepf 2012*a*; Brunet 2020). As illustrated in figure 1(*a*), dense canopies with closely packed elements effectively limit the penetration of the background turbulence, and the flow within is essentially sheltered from that above, except for a weak footprint of the mixing-layer eddies (Sharma & García-Mayoral 2020*b*). In contrast, as depicted in figure 1(*b*), sparse canopies with large element spacing allow the background turbulence to penetrate relatively unhindered into the canopy. Based on this, turbulence over sparse canopies has typically been considered a simple superposition of the wall-bounded flow and the element-induced flow, where the mean-velocity profile resembles that over a smooth wall (Huang *et al.* 2009; Pietri *et al.* 2009; Nepf 2012*a*). However, this argument is valid only when the drag induced by the canopy elements is negligible compared to the total drag. Recent direct numerical simulations (DNSs) have shown that even canopies with a frontal density as low as $\lambda_f \approx 0.01$ and spacing-to-height ratios as large as $s/h \approx 4$ can result in substantial element-induced drag, accounting for more than 60% of the total drag, and that such sparse canopies mainly modulate the background turbulence through their drag on the mean velocity profile, as the mean shear sets the scale of turbulence locally at each height (Sharma & García-Mayoral 2020*a*).

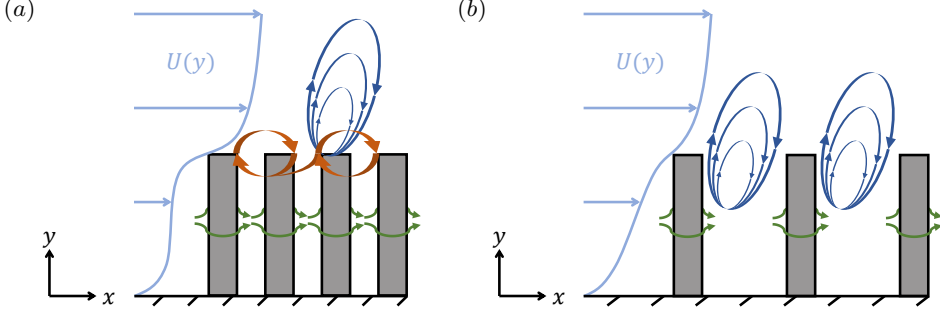


FIGURE 1. Graphical illustration of the flow regimes over (a) dense and (b) sparse canopies. The dark blue, orange and green arrows represent the background-turbulence eddies, mixing-layer-like eddies and element-induced eddies, respectively. Adapted from Poggi *et al.* (2004) and Sharma (2020).

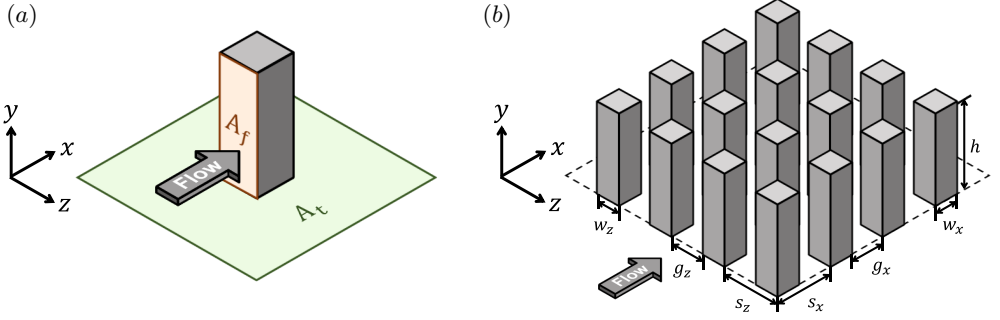


FIGURE 2. Schematic representation of (a) a canopy element and (b) a layout of canopy elements. In (a), A_f is the frontal area and A_t is the plan area occupied by the element. In (b), h is the element height; w_x , g_x and s_x are the element thickness, gap and spacing (pitch) in the streamwise direction, respectively, and w_z , g_z and s_z are those in the spanwise direction.

A popular quantity to characterise canopy density is the frontal density (Nepf 2012a), also known as the leaf area index in vegetated canopy literature (Wooding *et al.* 1973; Kaimal & Finnigan 1994),

$$\lambda_f = \frac{A_f}{A_t} = \int_0^h a(y) dy, \quad (1.1)$$

where A_f is the frontal area, A_t is the total plan area, h is the element height, $a(y) = w_z(y)/s^2$ is the frontal area per canopy volume, $w_z(y)$ is the element frontal width at each height, and s is the average spacing between elements, as depicted in figure 2(a). For prismatic canopies, the frontal density becomes $\lambda_f = w_z h / (s_x s_z)$, as shown in figure 2(b), where w , g and s are the element thickness, gap and spacing in the streamwise (x) or spanwise (z) direction. Nepf (2012a) noted that canopies are dense when $\lambda_f \gg 0.1$, sparse when $\lambda_f \ll 0.1$, and intermediate between the two limits. Permeability and porosity (ϕ) are also popular measures of density for denser canopies and other permeable substrates, embodying the ‘accessibility’ of the fluid region (Lightbody & Nepf 2006; Breugem *et al.* 2006; Luhar *et al.* 2008). However, these geometric parameters only provide a notional measure of canopy density, and occasionally fail to capture how different element arrangements can result in different flow regimes. The studies by Pietri *et al.* (2009) and Bailey & Stoll (2013) highlighted that identical density values of λ_f

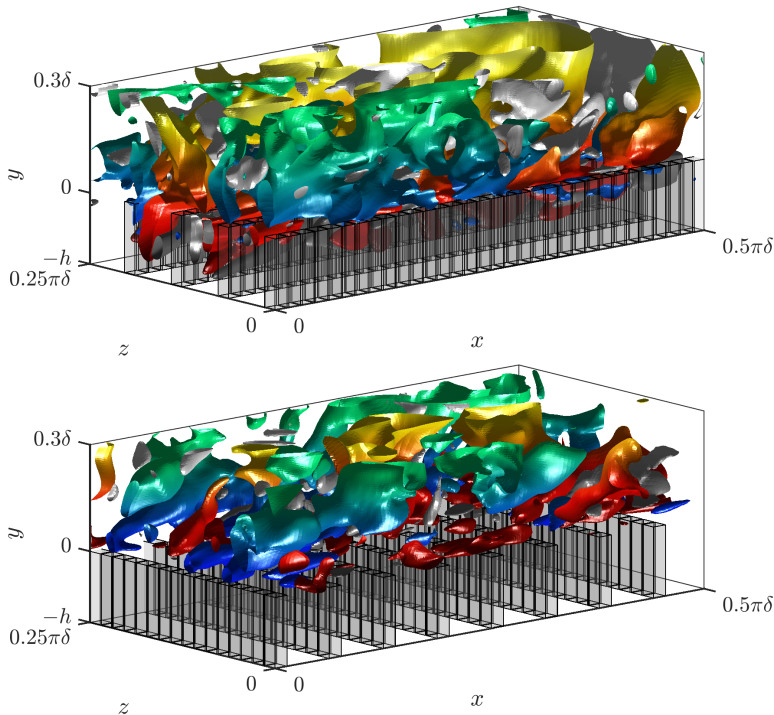


FIGURE 3. Instantaneous realisations of the $u'v'$ structures over and within canopies with the same number of elements per area and frontal density $\lambda_f \approx 0.91$: (a) streamwise-packed canopy $C_{S27 \times 108}$ with $s_x^+ \approx 27$, $s_z^+ \approx 108$ and $h^+ \approx 110$, and (b) spanwise-packed canopy $F_{S108 \times 27}$ with $s_x^+ \approx 108$, $s_z^+ \approx 27$ and $h^+ \approx 110$. The structures are coloured by distance to the floor, and consist of ejections ($u' < 0, v' > 0$ blue to green), sweeps ($u' > 0, v' < 0$ red to yellow), and outward and inward interactions ($u'v' > 0$ grey to white).

and ϕ do not necessarily translate to similar flow penetration behaviours and may not accurately reflect the actual canopy density regime. This limitation is illustrated in figure 3, depicting structures of intense $u'v'$ over canopies with the same number of elements and identical λ_f but different element layout, which are discussed in full detail in §4.1. As shown in figure 3(a), these structures penetrate more effectively into the streamwise-packed canopy compared to the spanwise-packed canopy in figure 3(b), showing that element layout, a factor not captured by λ_f , can significantly influence the canopy density regime. Sharma & García-Mayoral (2020a) argued that a canopy would be sparse if the spanwise spacing between elements is $s_z^+ \gtrsim 100$, which is large enough to fit in the near-wall streaks of characteristic width $\lambda_z^+ \approx 100$ (Kline *et al.* 1967; Kim *et al.* 1971). This is consistent with the observations of Poggi *et al.* (2004) and Huang *et al.* (2009), who noted a progressive departure from smooth-wall behaviour for sparse canopies as the spacing between elements decreases. However, Sharma & García-Mayoral (2020a) investigated only sparse canopies of isotropically laid filaments, and did not consider the effects of a wider variety of geometric parameters. Canopies that are clearly sparse or clearly dense were extensively investigated in Sharma & García-Mayoral (2020a) and Sharma & García-Mayoral (2020b), but the transition from one limit to the other was not addressed. This highlights the need for a more systematic approach to measure the extent of turbulence penetration, and to characterise canopy density. Recent studies have proposed to characterise canopy density as determined by the interchange between the

relative vertical positions of the zero-plane-displacement height (the depth perceived as the origin by the overlying turbulence) and the inflection in the mean velocity profile that occurs within the canopy (see e.g. Monti *et al.* 2020, and follow-up papers). The latter inflection occurs due to the near-bed boundary layer that forms in order for the mean flow to satisfy no-slip at the bed. The authors argued that this lower inflection played a key role in the flow dynamics, as it gave rise to an instability, reminiscent of Kelvin-Helmholtz, because the mean velocity profile satisfied Fjørtoft’s criterion for instability. The opposite is unfortunately the case: Fjørtoft’s criterion predicts instability for a mixing-layer type, concave-to-convex inflection, like the one at the canopy tips, and stability for convex-to-concave inflections like the one near the bed. Physically, the flow is the most unstable where the mean shear is maximum, and most stable where the shear is minimum. Furthermore, the lower inflection only occurs in canopy flows driven by a mean pressure gradient or a body force, as in this case a Darcy-like region of uniform velocity tends to form in the canopy core, requiring a Brinkman-like boundary layer at its bottom to meet no-slip at the bed. When the intra-canopy flow is driven mainly by the shear exerted by the overlying flow, as in zero-pressure-gradient boundary layers, the Darcy-flow contribution is non-existent, and there is therefore no inner inflection. A different approach is therefore necessary.

In the present study, we conduct DNSs of canopies with different layouts and element geometries. We aim to establish a metric for canopy density based on the flow dynamics to enable the quantitative diagnosis, characterisation and prediction of canopy density. For this, we quantify the extent and depth of the penetrating three-dimensional turbulence structures of intense Reynolds shear stress $u'v'$ (Del Alamo *et al.* 2006; Lozano-Durán *et al.* 2012). We focus on these structures because they are responsible for momentum transport and turbulence diffusion between the overlying and the canopy regions, and are ultimately responsible for the wall-normal distribution of the Reynolds stress and thus the shape of the mean-velocity profile. Based on this measure, we explore the influence of the different geometric characteristics of the canopy on whether turbulence penetrates or not, and identify which are the key ones to determine canopy density. The paper is organised as follows. §2 presents the numerical method and the different canopies simulated. §3 introduces and discusses the metrics used to measure turbulence penetration. §4 presents the DNS results, focusing on how different canopy parameters affect turbulence penetration. Finally, §5 summarises the conclusions of our investigation.

2. Methodology

In this section, we briefly discuss the DNS method in §2.1, and present the relevant parameters for the canopies simulated, with different element geometry and layout, in §2.2.

2.1. Direct numerical simulations

We carry out DNS of closed symmetric channels with rigid filament canopies protruding from both walls. The simulations are conducted within a coordinate system where x , z , and y represent the streamwise, spanwise, and wall-normal directions, respectively. The filament canopies and the numerical domain studied are portrayed in figure 4, where $\delta = 1$ is the channel half-height measured from the channel centre to the canopy-tip planes. The canopy elements extend below $y = 0$ on the bottom wall and above $y = 2\delta$ on the top wall. The wall-parallel size for all simulations is no smaller than $2\pi\delta$ in the streamwise direction and $\pi\delta$ in the spanwise direction, with the largest size extending to $2.8\pi\delta \times 1.4\pi\delta$.

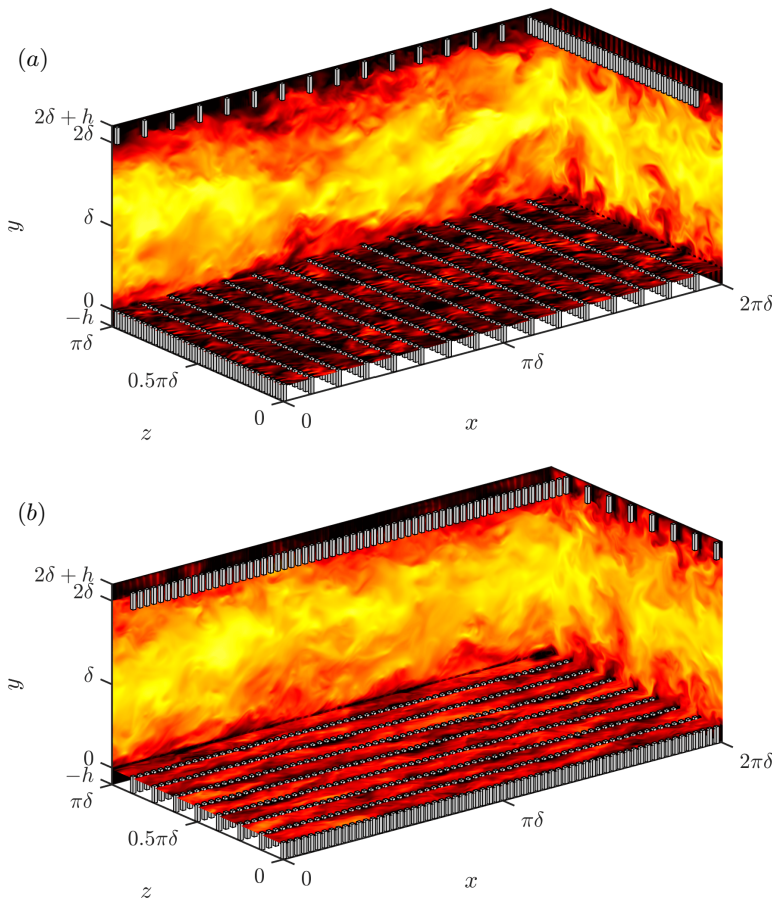


FIGURE 4. Schematics of the numerical channel for (a) spanwise-packed canopy $F_{S216 \times 54}$, with $s_x^+ \approx 216$, $s_z^+ \approx 54$ and $h^+ \approx 110$, and (b) streamwise-packed canopy $C_{S54 \times 216}$, with $s_x^+ \approx 54$, $s_z^+ \approx 216$ and $h^+ \approx 110$. Details of the canopy geometries are presented in table 1. An instantaneous realisation of the streamwise velocity is shown in axis-orthogonal planes.

The DNS code in this study is from Sharma & García-Mayoral (2020*a,b*) and has been validated in Sharma (2020) and Chen & García-Mayoral (2023). It is summarised here for reference. The numerical method resolves the three-dimensional incompressible Navier-Stokes equations,

$$\frac{\partial \mathbf{u}}{\partial t} + \mathbf{u} \cdot \nabla \mathbf{u} = -\nabla p + \frac{1}{Re} \nabla^2 \mathbf{u}, \quad (2.1)$$

$$\nabla \cdot \mathbf{u} = 0, \quad (2.2)$$

where $\mathbf{u} = \langle u, w, v \rangle$ is the velocity vector with components in the streamwise, spanwise and wall-normal directions, respectively, p is the kinematic pressure, and Re denotes the bulk Reynolds number $Re = U_b \delta / \nu$ based on the bulk velocity U_b , the channel half-height δ , and the kinematic viscosity ν . The simulation is operated at a constant mean pressure gradient, with the flow rate adjusted to achieve the targeted friction Reynolds number $Re_\tau = u_\tau \delta / \nu \approx 180 - 2000$, where u_τ is the reference friction velocity evaluated at the canopy-tip plane. No-slip and impermeability boundary conditions are applied at both channel walls. The rigid elements are resolved using a direct-forcing, immersed-

boundary method (Mittal & Iaccarino 2005; García-Mayoral & Jiménez 2011). In this work, variables scaled with u_τ and ν are termed as in inner units, denoted by superscript $(\cdot)^+$, and those scaled with U_b and δ are referred to as in outer units.

In the wall-normal direction, a second-order central difference scheme is applied on a staggered grid. At the channel centre, where the mean shear is the weakest, the stretched wall-normal grid has a resolution $\Delta y_{max}^+ \approx 3.0$ when $Re_\tau \approx 180$. At higher Reynolds numbers, where dissipation occurs at larger scales (Jiménez 2012), Δy_{max}^+ extends from 3.6 to 7.0 as Re_τ increases from 360 to 2000. The finest resolution Δy_{min}^+ is at the floor or canopy-tip plane, wherever the mean shear is the greatest. For all cases, $\Delta y_{min}^+ \lesssim 0.3$ is satisfied when scaled with the local, dynamically relevant friction velocity, as proposed in Sharma & García-Mayoral (2018, 2020a).

To balance computational cost and resolution, the numerical domain is divided into blocks with different wall-parallel resolutions (García-Mayoral & Jiménez 2011). The wall blocks, containing the roughness sublayer, have a finer resolution than the block encompassing the channel centre. In the finer blocks, the grid resolution resolves not only the turbulent scales but also the canopy geometry and the element-induced eddies, which are typically of the order of or smaller than the element thickness (Poggi *et al.* 2004). Consequently, the wall-parallel grid spacings in x and z are smaller than w_x^+ and w_z^+ . Sharma & García-Mayoral (2020b) examined wall-parallel resolutions for dense canopies, and concluded that a marginal resolution of 9 points per spacing and 3 points per element width for a filament canopy with $s^+ \approx 24$, $w^+ \approx 5$ and $h^+ \approx 100$ could underestimate the turbulent fluctuation within the canopy, with a maximum deviation of up to 20% observed in the wall-normal fluctuations, although this discrepancy reduced to 4% just above the tips. In our case, the most resolution-demanding simulations are typically those with relatively thin elements or narrow gaps, where small grid spacings are required to resolve the canopy geometry or the fluid in-between elements. In table 1, the canopy with thinnest filaments is G41_{S47×47}, with $w_x^+ = w_z^+ \approx 6$ and $s_x^+ = s_z^+ \approx 47$, which is simulated with a resolution $\Delta x^+ = \Delta z^+ \approx 2$. For canopy IS2000_{G30×30} at $Re_\tau \approx 2000$, with $w_x^+ = w_z^+ \approx 24$ and $s_x^+ = s_z^+ \approx 54$, the resolution is also marginal at $\Delta x^+ = 6$ and $\Delta z^+ \approx 3$. Such marginal resolutions are applied only for the densest canopy cases, for which fluctuations within the canopy are in any event weak compared to above, and thus higher resolutions do not change the behaviour observed. For all other canopies, a minimum of 16 points per streamwise or spanwise pitch are used. The height of the fine blocks is chosen such that the small and rapid element-induced eddies decay naturally before approaching the coarse block at the channel centre, which has a standard smooth-wall resolution of $\Delta x^+ \approx 8$ and $\Delta z^+ \approx 4$ (Jiménez & Moin 1991). The height above the canopy tips of the fine-resolution blocks is set to at least twice the element width for sparse canopies and twice the gap size for dense canopies, correlating with the height of the roughness sublayer (Chen & García-Mayoral 2023). This is validated *a posteriori* by examining the spectral densities of turbulent fluctuations to ensure that any small-wavelength signal has already vanished well below the inter-block interface.

2.2. Simulation parameters

We consider flows over canopies with rigid prismatic elements to thoroughly investigate turbulence penetration across various canopy layouts, element geometries and Reynolds numbers. Figure 2 illustrates the morphology of the canopies studied, and table 1 details the relevant simulation parameters. We note that in the literature, the terms ‘spacing’ and ‘gap’ are sometimes used interchangeably, mainly in the context of canopies with thin filaments, where the element width w is small compared to both s and g , so that $s = g + w \approx g$ (Cui *et al.* 2003; Bailey & Stoll 2013). Here, we consider both thin filaments

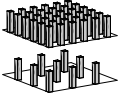
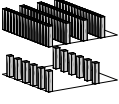
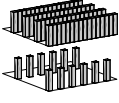
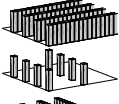
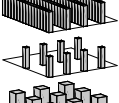
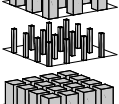
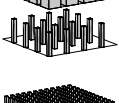
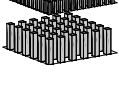
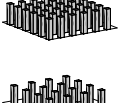
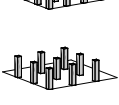
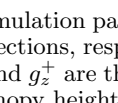
		Case	$N_x \times N_z$	Re_τ	λ_f	s_x^+	g_x^+	s_z^+	g_z^+	h^+
Isotropic		IS36×36	96×48	550.2	2.04	36.0	12.0	36.0	12.0	110.0
		IS54×54 ¹	64×32	549.7	0.91	54.0	30.0	54.0	30.0	109.9
		IS72×72	48×24	548.2	0.51	71.8	47.8	71.8	47.8	109.6
		IS108×108 ²	32×16	548.7	0.23	107.7	83.8	107.7	83.8	109.7
		IS144×144	24×12	546.9	0.13	143.2	119.3	143.2	119.3	109.4
		IS216×216 ³	16×8	550.7	0.06	216.3	192.2	216.3	192.2	110.1
		IS288×288	12×6	551.1	0.03	288.5	264.5	288.5	264.5	110.2
		IS432×432	8×4	549.4	0.01	431.5	407.6	431.5	407.6	109.9
Fence		FS108×27 ⁴	32×64	548.9	0.91	107.8	83.8	26.9	3.0	109.8
		FS144×36	24×48	548.7	0.51	143.7	119.7	35.9	12.0	109.7
		FS216×54	16×32	553.4	0.23	217.3	193.2	54.3	30.2	110.7
		FS288×72	12×24	548.3	0.13	287.1	263.1	71.8	47.8	109.7
		FS432×108	8×16	548.9	0.06	431.1	407.1	107.8	83.8	109.8
Canyon		CS27×108 ⁵	128×16	552.9	0.91	27.1	3.0	108.6	84.4	110.6
		CS36×144	96×12	549.8	0.51	36.0	12.0	143.9	119.9	110.0
		CS54×216	64×8	553.6	0.23	54.3	30.2	217.4	193.2	110.7
		CS72×288	48×6	550.0	0.13	72.0	48.0	288.0	264.0	110.0
		CS108×432	32×4	548.5	0.06	107.7	83.8	430.8	406.9	109.7
Fixed s_z ($s_z^+ = 108$)		ZS27×108 ⁵	128×16	552.9	0.91	27.1	3.0	108.6	84.4	110.6
		ZS108×108 ²	32×16	548.7	0.23	107.7	83.8	107.7	83.8	109.7
		ZS216×108	16×16	548.8	0.11	215.5	191.6	107.8	83.8	109.8
Fixed s_x ($s_x^+ = 108$)		XS108×27 ⁴	32×64	548.9	0.91	107.8	83.8	26.9	3.0	109.8
		XS108×108 ²	32×16	548.7	0.23	107.7	83.8	107.7	83.8	109.7
		XS108×216	32×8	548.0	0.11	107.6	83.7	215.2	191.3	109.6
Fixed gap ($g^+ \approx 41$)		G41S66×66	48×24	360.7	0.63	66.1	41.3	66.1	41.3	110.2
		G41S53×53	48×24	359.7	0.46	53.0	41.2	53.0	41.2	109.9
		G41S47×47 ⁶	48×24	360.3	0.29	47.2	41.3	47.2	41.3	110.1
Fixed pitch ($s^+ \approx 47$)		S47G14×14	48×24	360.1	1.61	47.1	14.7	47.1	14.7	110.0
		S47G27×27	48×24	361.1	1.02	47.3	26.6	47.3	26.6	110.3
		S47G35×35	48×24	359.6	0.58	47.1	35.3	47.1	35.3	109.9
		S47G41×41 ⁶	48×24	360.3	0.29	47.2	41.3	47.2	41.3	110.1
Outer-similar geometry		OS180G15×15	48×24	179.8	0.70	23.5	14.7	23.5	14.7	44.1
		OS360G30×30	48×24	360.3	0.70	47.2	29.5	47.2	29.5	88.4
		OS720G60×60	48×24	725.5	0.70	95.0	59.4	95.0	59.4	178.0
		OS1080G90×90	48×24	1084.6	0.70	142.0	88.7	142.0	88.7	266.2
Inner-similar geometry		IS550G30×30 ¹	64×32	549.7	0.91	54.0	30.0	54.0	30.0	109.9
		IS900G30×30	96×48	950.8	0.91	54.0	30.0	54.0	30.0	110.1
		IS2000G30×30	192×96	1991.9	0.91	53.8	29.9	53.8	29.9	109.6
		IS550G84×84 ²	32×16	548.7	0.23	107.7	83.8	107.7	83.8	109.7
		IS900G84×84	48×24	923.7	0.23	110.2	85.7	110.2	85.7	112.2
		IS2000G84×84	96×48	1974.0	0.23	111.8	87.0	111.8	87.0	113.9
		IS550G192×192 ³	16×8	550.7	0.06	216.3	192.2	216.3	192.2	110.1
		IS900G192×192	32×16	895.2	0.06	223.0	198.2	223.0	198.2	113.5
		IS2000G192×192	48×24	1934.2	0.06	228.8	203.4	228.8	203.4	116.4

TABLE 1. Simulation parameters. N_x and N_z are the numbers of elements in the streamwise and spanwise directions, respectively; Re_τ is the friction Reynolds number; λ_f is the frontal density; s_x^+ , s_z^+ , g_x^+ and g_z^+ are the pitch and gap in the streamwise and spanwise directions, respectively; h^+ is the canopy height. Cases with the same superscript are the same DNS.

($w/s \approx 0.06$) and thick and densely-packed elements ($w/s \approx 0.67$). To avoid confusion, we refer to the ‘spacing’ s , the sum of the gap and element width, as the ‘pitch’ in the remainder of this work.

All canopies investigated consist of collocated prismatic elements with a square wall-parallel cross-section, where $w_x^+ = w_z^+$. To distinguish among different simulations, the prefix indicates the canopy characteristics, and the subscript denotes the approximate streamwise and spanwise spacing/pitch (‘S’) or gap (‘G’) in inner units. For example, case C_{S27×108} refers to a canopy resembling a ‘Canyon’ with streamwise-packed elements, where $s_x^+ \approx 27$ and $s_z^+ \approx 108$.

In table 1, the first five groups consist of canopies with identical element geometry, where $h^+ \approx 110$ and $w_x^+ = w_z^+ \approx 24$, but with different pitches and gaps. The first group, prefixed with ‘I’, consists of isotropic canopies with equal streamwise and spanwise pitches $s_x^+ = s_z^+$. These isotropic canopies are from Chen & García-Mayoral (2023), which showed that turbulence effectively penetrates the sparse canopy I_{S432×432} and perceives an origin at the floor, while turbulent eddies ‘skim’ over the dense canopy I_{S36×36} and perceives a smooth wall at the tips. The second and third groups consist of fence-like canopies prefixed with ‘F’, with spanwise-packed elements, and canyon-like canopies prefixed with ‘C’, with streamwise-packed elements, each matching the total number of posts of isotropic canopies I_{S54×54} to I_{S216×216} and therefore the value of λ_f . It will be demonstrated in §4.1 that canopies with the same λ_f can result in different turbulence penetration behaviours, depending on whether the elements are more closely distributed in the streamwise or spanwise direction. In the fourth group, marked by ‘Z’, we gradually reduce the number of posts in the streamwise direction N_x from the canyon-like canopy C_{S27×108}, keeping all spanwise parameters (N_z , s_z^+ and g_z^+) fixed. Similarly, the fifth group, denoted by ‘X’, consists of canopies with different N_z but with the same streamwise parameters. In §4.2, with the ‘Z’ and ‘X’ groups, we investigate whether parameters in the streamwise or spanwise direction have more impact on flow penetration. To identify whether the gap or pitch matters, we study canopies with a fixed gap but different pitch (group ‘G’) or with a fixed pitch but different gap (group ‘S’) in §4.3. The number that follows prefixes ‘G’ and ‘S’ denotes the approximate value of the fixed gap and pitch in inner units, respectively. Finally, in §4.4, we investigate the effect of the Reynolds number using canopies with similar geometry in outer (same s/δ , g/δ and h/δ in group ‘OS’) or inner units (same s^+ , g^+ and h^+ in group ‘IS’).

3. Measuring the penetration of turbulence into the canopy

Before we embark in the analysis of canopy density, we need to establish how to measure turbulence penetration from the overlying flow. In §3.1, we first discuss how we identify the penetrating structures that contribute to the momentum and turbulence transport in the vicinity of the canopy-tip plane. In §3.2, we introduce the metrics that we will use to quantify the penetration of these structures.

3.1. Identification of background structures

To investigate turbulence penetration, we focus on structures of intense pointwise $u'v'$ from the overlying flow, because of their importance in momentum transport. The Reynolds shear stress $u'v'$ can be categorised into four quadrants depending on the signs of the fluctuating velocity components u' and v' (Wallace *et al.* 1972; Willmarth & Lu 1972; Lozano-Durán *et al.* 2012; Lozano-Durán & Jiménez 2014). The quadrants Q1, Q2, Q3, and Q4 represent outward interactions ($u' > 0, v' > 0$), ejections ($u' < 0, v' > 0$), inward interactions ($u' < 0, v' < 0$), and sweeps ($u' > 0, v' < 0$), respectively.

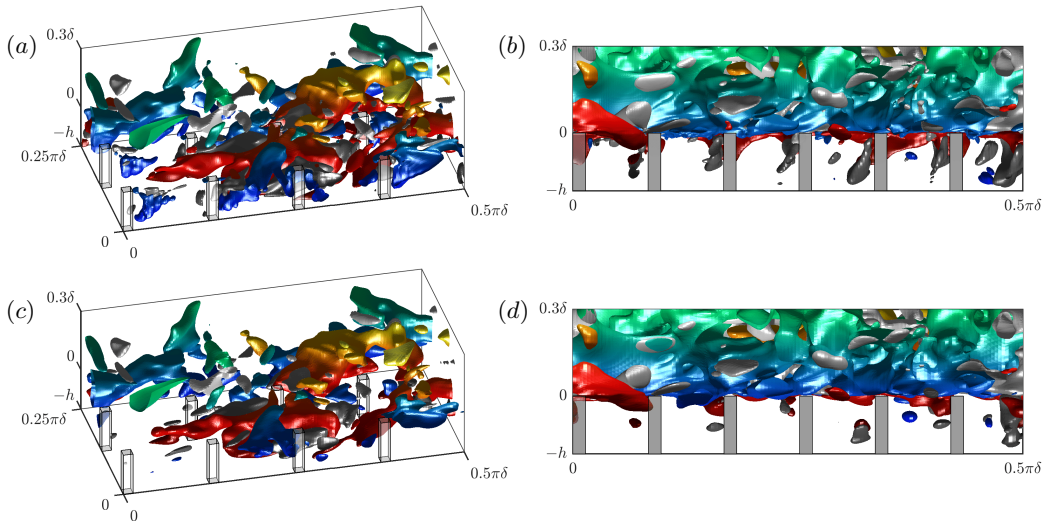


FIGURE 5. Instantaneous realisations of $u'v'$ structures for (a, c) case $\text{Is}_{216 \times 216}$ and (b, d) case $\text{FS}_{144 \times 36}$. Structures are coloured by distance to the floor, ejections in blue to green, sweeps in red to yellow, and outward and inward interactions in grey to white. (a, b), raw flow fields; (c, d), flow fields spectrally filtered to remove the element-induced, coherent flow.

Depending on the density regime, turbulent structures from different quadrants can have different intensities and locations (Brunet 2020). For certain canopies, the element-induced structures can merge with the background structures from the overlying flow, which may misleadingly suggest that the background turbulence penetrates deeply into the canopy. To prevent this, we filter out the element-coherent signal spectrally to isolate the background structures.

As depicted in figure 5(a), element-induced coherent flows typically are formed by stem-scale eddies in the wake of each obstacle. A similar pattern for stem-scale eddies is also observed in Poggi *et al.* (2004) and Sharma & García-Mayoral (2020a) for sparse canopies. As shown in figure 5(b), element-induced top-shedding eddies can also form. Note that the latter are different from the canopy-scale, mixing-layer-like eddies induced by the inflectional mean profile (Raupach *et al.* 1996; Nepf 2012a). The element-induced, coherent flows shown in figures 5(a, b) are not part of the penetrating turbulence from the overlying background flow, and we therefore filter them out before measuring turbulence penetration. A conventional method to obtain the background flow is through triple decomposition (Reynolds & Hussain 1972),

$$\mathbf{u}(x, y, z, t) = \mathbf{U}(y) + \mathbf{u}'(x, y, z, t), \quad (3.1)$$

$$\mathbf{u}'(x, y, z, t) = \tilde{\mathbf{u}}(x, y, z) + \mathbf{u}''(x, y, z, t), \quad (3.2)$$

where \mathbf{U} is the mean velocity profile, and \mathbf{u}' is the full temporal and spatial turbulent fluctuation. The latter can be further decomposed into a time-averaged but spatially varying component, $\tilde{\mathbf{u}}$, and the remaining time-varying fluctuation, \mathbf{u}'' . Abderrahaman-Elena *et al.* (2019) carried out DNSs for small-to-intermediate roughness with $h^+ \lesssim 35$, showing that the element-induced flow is modulated in amplitude by the overlying background turbulence. However, as roughness size increases, wake unsteadiness intensifies, complicating the isolation of the background flow (Abderrahaman-Elena *et al.* 2019). For the present canopies, with sizes up to $h^+ \approx 266$ and $w^+ \approx 32$, there is significant unsteady

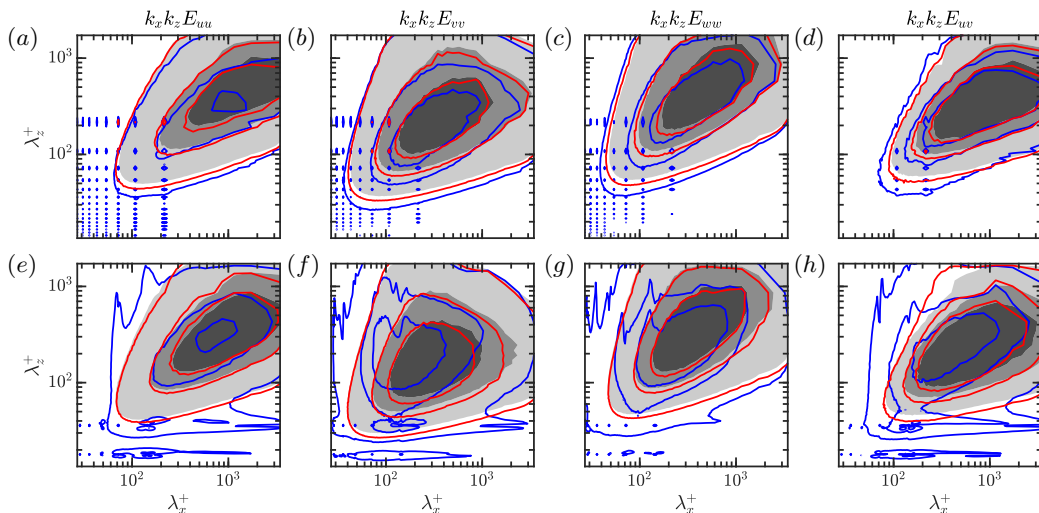


FIGURE 6. Spectral energy densities for (a, b, c, d) case $\text{IS}_{216 \times 216}$ and (e, f, g, h) case $\text{FS}_{144 \times 36}$. The blue, red and shaded contours are at heights $y^+ = (0, 1, 2)l_d^+$ above the tips, respectively, where $l_d^+ = w^+ \approx 24$. The contours are at 0.01, 0.05 and 0.1 times the r.m.s. level.

yet element-coherent flow, rendering equation (3.2) ineffective as the time-dependent element-wake flow cannot be accurately represented by the temporally averaged term $\tilde{\mathbf{u}}$.

As a practical approximation, we thus use a spectral filter to isolate the background flow, aiming to retain most of the energy of the background-turbulent wavelengths while removing the element-induced signal. As shown in figures 6(a-d), the element-induced footprint appears as concentrated energy at the canopy pitch and its harmonics. This footprint decays naturally with height above the canopy-tip plane, leaving only the background-turbulence wavelengths. Thus, we can use these background wavelengths to construct a spectral filter that selectively removes the element-induced signal while retaining the background flow field. To establish this filter, we first identify the height at which the element-induced signal has decayed naturally. Near the tips, the scale of the element-induced eddies is generally determined by the element width or gap, which provides the size of the ‘active’ region for canopy-turbulence interaction (Sharma & García-Mayoral 2020b). When the element width is larger than the gap ($w^+ > g^+$), the texture-induced eddies are approximately of the size of the element width (Poggi *et al.* 2004; Sadique *et al.* 2017; Sharma & García-Mayoral 2020a). Conversely, when the gap is larger than the element width ($w^+ < g^+$), the texture-induced eddies are approximately of the size of the gap (MacDonald *et al.* 2018). Thus, the reference height for the spectral filter depends on a ‘decay length’, defined as $\ell_d^+ = \min(w^+, g^+)$. For our anisotropic canopies with $s_x \neq s_z$, we use $\ell_d^+ = w^+$ for simplicity. As shown in figure 6, the element-induced footprint essentially vanishes at a height of two ‘decay lengths’, $y^+ \approx 2\ell_d^+ \approx 48$, above both the isotropic canopy $\text{IS}_{216 \times 216}$ and the fence-like canopy $\text{FS}_{144 \times 36}$, suggesting that this as a suitable reference height to capture the background signal alone.

As depicted in figures 7(a, e), the filter removes the energy at the canopy pitch and its harmonics, while retaining the main spectral ‘lobe’ of background wavelengths. The energy within the background ‘lobe’ accounts for 97% of $(u^+)^2$ and $(v^+)^2$, respectively, as shown in figures 7(a, e). Care must be taken when choosing this filter percentage because if too many wavelengths remain unfiltered, too little element-induced, coherent flow is removed. However, if too many wavelengths are removed, the background flow

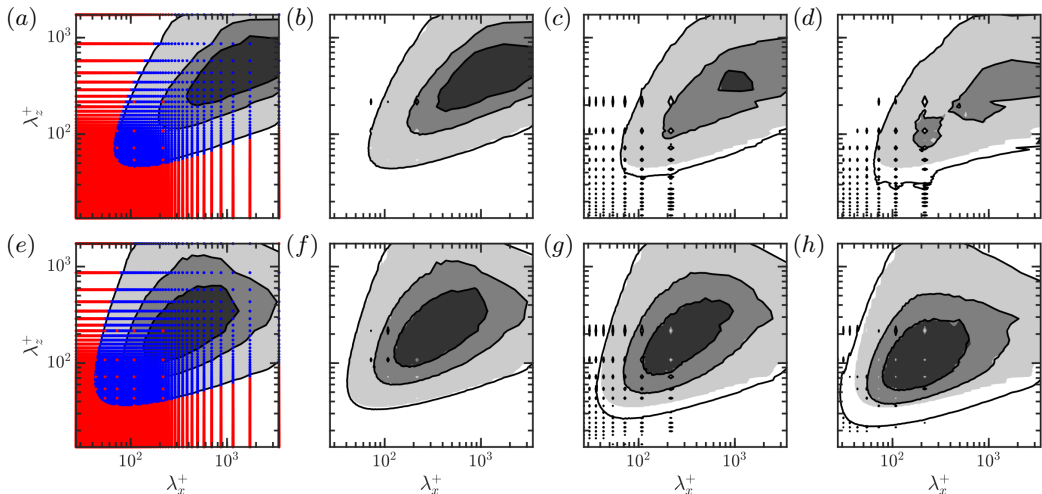


FIGURE 7. Spectral filters and spectral energy densities for case $\text{IS}_{216 \times 216}$, with $h^+ \approx 110$ and $l_d^+ \approx w^+ \approx 24$. Contours from left to right represent energy densities at $y^+ \approx 48, 24, 0$ and -55 ; (a, b, c, d), $k_x k_z E_{uu}$; and (e, f, g, h), $k_x k_z E_{vv}$. Line contours represent the energy density of the raw velocity, and shaded contours that of the filtered flow fields. The filters are shown in (a, e), where red dots indicate the wavelengths filtered-out and blue dots those retained, containing up to 97% of the total $(u'^+)^2$ and $(v'^+)^2$, respectively. The contour levels are 0.01, 0.05 and 0.1 times the r.m.s. level.

within the substrate can be distorted or significantly reduced, artificially removing the signature of the eddies that are actually penetrating. A sensitivity analysis for the filter is provided in appendix A for reference.

The spectral filter is applied within the canopy region ($y^+ \leq 0$) to remove the element-induced flow, while it is switched off at height $y^+ \geq 2\ell_d^+$, where the element-induced flow has already decayed. To avoid an abrupt transition, we apply a half-Hanning window for the filter intensity at height $0 \leq y^+ \leq 2\ell_d^+$, gradually reducing the filtered energy from 100% at $y^+ \leq 0$ to 0% at $y^+ \geq 2\ell_d^+$ for each filtered wavelength. As illustrated in figure 7, the proposed filter removes the energy in the canopy harmonics and the quiescent wavelengths. We note that this also removes any background-turbulence signal that may exist at the canopy harmonics, but this contribution is generally small compared to the remainder. The instantaneous realisations of the filtered flow field in figures 5(c, d) illustrate that both the stem-scale eddies of the sparse canopy $\text{IS}_{216 \times 216}$ and the shedding eddies of the fence-like canopy $\text{FS}_{144 \times 36}$ are effectively removed, while the background turbulent eddies remain essentially unmodified. In figure 5(c), the applied filter slightly reduces the volume of the largest structure by approximately 5% compared to its original size in figure 5(a), which we deem acceptable. For case $\text{FS}_{144 \times 36}$ in figures 5(b, d), the large structures remain essentially unaffected by the spectral filter, as they do not significantly penetrate within the ‘fences’ in any event.

After filtering the element-induced, coherent flow, we define the background structures that contribute the most to the Reynolds shear stress as connected regions satisfying

$$|u'v'(x, y, z)| > H\tau_{tip}, \quad (3.3)$$

where $u'v'(x, y, z)$ is the pointwise Reynolds shear stress, and H is a threshold scaled with the total shear stress evaluated at the canopy tips τ_{tip} . The connectivity between points is determined based on the six orthogonal neighbours in the Cartesian grid of the simulation.

The choice of the right-hand side in (3.3) significantly influences the resulting topology of the eddies. A low threshold value can result in large, interconnected eddies spanning the entire flow field, while an excessively high threshold may filter out too many eddies, leaving only a thin skeleton for the most intense ones (Nagaosa & Handler 2003; Del Alamo *et al.* 2006). In smooth-wall studies, three-dimensional flow structures are typically identified using height-dependent normalisation factors (Jiménez 2018; Marusic & Monty 2019). For example, the early work of quadrant analysis by Willmarth & Lu (1972) used the mean Reynolds shear stress at each height,

$$|u'v'(x, y, z)| > H_{u'v'(y)} |\overline{u'v'(y)}|. \quad (3.4)$$

However, this approach encounters a limitation when $|\overline{u'v'(y)}|$ tends toward zero near the channel centre, leading to an exaggerated representation of the eddies in this region. This limitation could be circumvented by using the r.m.s. of velocity fluctuations $u'(y)$ and $v'(y)$, as in Wallace *et al.* (1972), Lu & Willmarth (1973) and Bogard & Tiederman (1986),

$$|u'v'(x, y, z)| > H_{u'(y)v'(y)} u'(y)v'(y), \quad (3.5)$$

or the r.m.s. of Reynolds stress fluctuation (Narasimha *et al.* 2007),

$$|u'v'(x, y, z)| > H_{(uv)'(y)} (uv)'(y). \quad (3.6)$$

In the present case, the height-dependent normalisation factors $|\overline{u'v'(y)}|$, $u'(y)v'(y)$ and $(uv)'(y)$ in (3.4-3.6) decrease rapidly within the canopy, which would result in an over-representation of the eddies within. Abderrahaman-Elena *et al.* (2019) and Sharma & García-Mayoral (2020b) have reported that turbulent fluctuations decay exponentially within the canopy, with the slowest decay occurring for the wall-normal component v' . However, persistent footprints of Kelvin-Helmholtz rollers are still observed at half-height below the tips for a dense canopy with $\lambda_f \approx 4.6$ and $h^+ \approx 100$ (Sharma & García-Mayoral 2020b). Consequently, as the normalisation factors on the right-hand side of (3.4-3.6) become vanishingly small within a dense canopy, weak fluctuations could be identified as strong eddies, with their significance overemphasised. To avoid this, we normalise the pointwise Reynolds shear stress with a y -constant value, as indicated in (3.3), using the total shear stress at the canopy-tip plane, τ_{tip} . This normalisation factor allows a consistent statistical analysis of canopies across various density regimes using a constant H , circumventing the need to recalibrate the value of H for each canopy, as τ_{tip} provides the scale for the flow in the vicinity of the tips for both dense and sparse canopies. In contrast, alternative normalisation factors, such as $u'v'(y_{tip})$ and $u'(y_{tip})v'(y_{tip})$, can yield large values for H for dense canopies and small values for sparse canopies, complicating the comparative analysis across different canopies.

The value of the threshold H in (3.3) is determined based on a percolation analysis (Del Alamo *et al.* 2006), as depicted in figure 8. At high values of H ($H \gtrsim 3$), only a few eddies, corresponding to the core of the most intense structures, are identified. As H decreases, new structures are identified while the existing ones expand in size. For $H \lesssim 3$, the largest eddy expands proportionally with the total volume, and the volume ratio between the largest eddy and all eddies, V_{lar}/V_{tot} , remains roughly constant. As H continues to decrease, the identified objects begin to merge, significantly increasing the ratio V_{lar}/V_{tot} . For $H \lesssim 1$, the total number of eddies, normalised with its maximum, N/N_{max} decreases, and V_{lar}/V_{tot} approaches unity as most of the volume is concentrated within the largest eddy. Figure 8 illustrates that a percolation crisis occurs when $0.5 \lesssim H \lesssim 3$ for all cases. We therefore use $H = 1.6$ throughout to ensure that individual

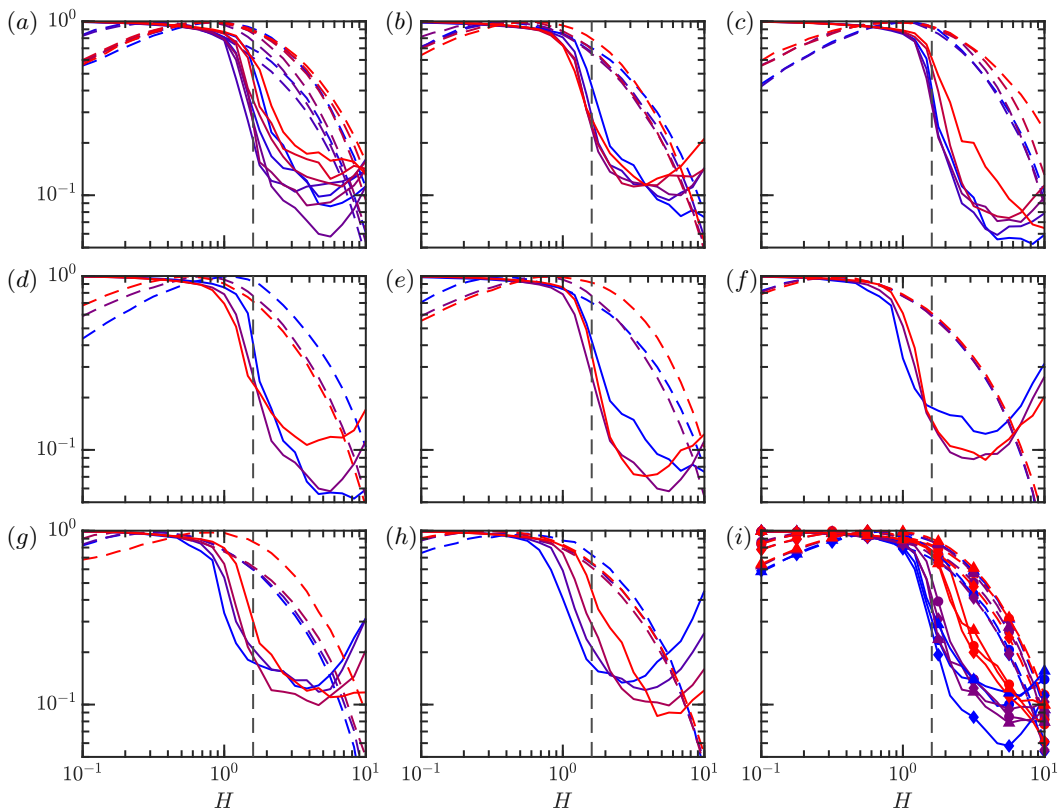


FIGURE 8. Percolation diagram for the identification of $u'v'$ structures. (a) canopies with isotropic layout; (b) fence-like layout; (c) canyon-like layout; (d) fixed s_z ; (e) fixed s_x ; (f) fixed gap; (g) fixed pitch; (h) similar geometry in outer units; and (h) similar geometry in inner units. From blue to red, the lines represent canopies with decreasing λ_f in (a-g) and increasing Re_τ in (h,i). The solid lines represent the volume ratio between the largest eddy and the total volume of all eddies, V_{lar}/V_{tot} ; the dash-dotted lines represent the ratio of the number of identified eddies to the maximum number of eddies, N/N_{max} ; and the vertical dashed lines represent the chosen threshold $H = 1.6$. In (i), lines marked with \bullet , \blacklozenge , \blacktriangle , are cases with the same geometry as cases IS550_{G30×30}, IS550_{G84×84} and IS550_{G192×192}, respectively.

structures remain separate while avoiding excessive volume shrinkage. In appendix B, it is shown that for H within the range of the percolation crisis, the size and location of the penetrating eddies are largely insensitive to the exact choice of H . Although the eddy volume at each height increases slightly for larger H , the penetration depth remains unaffected.

3.2. Metrics for the penetration of background-turbulence structures

So far, we have isolated the background turbulent structures from the full flow field through filtering and a percolation analysis. From here on we will focus on the penetrating structures that cross the canopy-tip plane, as they embody turbulence penetration from above. In this subsection, we introduce measures for the location, span and volume of these ‘tip-plane-intersecting’ structures, which we will refer to as ‘interfacial eddies’, aiming to characterise the extent and depth of their penetration into the canopy.

The mean location of a structure can be characterised by the centroid position of its

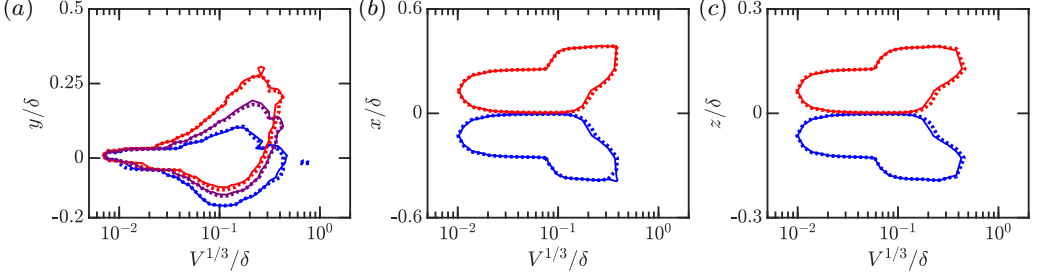


FIGURE 9. Probability density function of the spatial distribution of interfacial eddies of intense $u'v'$ for canopy $IS_{216 \times 216}$. The solid and dotted contour lines represent statistics for the volume and the density of $u'v'$, respectively, and enclose 95% of the penetrating eddies; the red, purple and blue lines represent the locations of the 25th percentile, the centroid and the 75th percentile, respectively. In the wall-parallel directions, the percentile locations are offset by their corresponding centroid.

volume,

$$\mathbf{x}_{c,vol} = \frac{\int_{\Omega} \mathbf{x}(x, y, z) dV}{\int_{\Omega} dV}, \quad (3.7)$$

and also by the centroid position of its $u'v'$ distribution,

$$\mathbf{x}_{c,uv} = \frac{\int_{\Omega} u'v'(x, y, z) \mathbf{x}(x, y, z) dV}{\int_{\Omega} u'v'(x, y, z) dV}, \quad (3.8)$$

where \mathbf{x} is the pointwise position vector for all contiguous points within the volume of the structure, Ω . The spatial extent of a structure can be characterised by its maximum (\mathbf{x}_{max}) and minimum (\mathbf{x}_{min}) position in x, y and z , respectively. However, we typically observe that eddies are irregular, so the absolute top and bottom do not necessarily provide information about where the majority of the volume and $u'v'$ are located. To quantify the spatial distribution of eddies, we instead measure the position of the n th percentile for volume ($\mathbf{x}_{nth,vol}$),

$$\frac{\int_{\mathbf{x}_{min}}^{\mathbf{x}_{nth,vol}} \mathbf{x}(x, y, z) dV}{\int_{\Omega} dV} = \frac{n}{100}, \quad (3.9)$$

and the position of the n th percentile based on $u'v'$ intensity ($\mathbf{x}_{nth,uv}$),

$$\frac{\int_{\mathbf{x}_{min}}^{\mathbf{x}_{nth,uv}} u'v'(x, y, z) dV}{\int_{\Omega} u'v'(x, y, z) dV} = \frac{n}{100}. \quad (3.10)$$

An eddy with $y_{min} = 0.1\delta$, $y_{5th,uv} = 0.3\delta$, $y_{95th,uv} = 0.5\delta$ and $y_{max} = 0.6\delta$, for instance, would have an absolute extent in y from $y = 0.1\delta$ to $y = 0.6\delta$, but 90% of its total $u'v'$ stress would be concentrated between $y = 0.3\delta$ and $y = 0.5\delta$, with only 5% above and below. We denote the span of this $u'v'$ -concentrated region as $y_{90,uv}^+ = y_{95th,uv}^+ - y_{5th,uv}^+ = 0.2\delta$. As an example, figure 9 portrays the typical location of the centroid and the 25th and 75th percentiles for the penetrating eddies for a sparse canopy. As shown in panel (a), of the interfacial eddies, small ones of size $V^{1/3}/\delta \lesssim 0.03$ tend to remain near the tips, as they cannot extend too much above or below this region due to their small size. Meanwhile, the larger eddies, of size $V^{1/3}/\delta \gtrsim 0.2$, can effectively penetrate into the canopy, as well as extend well above the tips. On average, the interfacial eddies extend symmetrically in the wall-parallel directions, x and z , as shown in figures

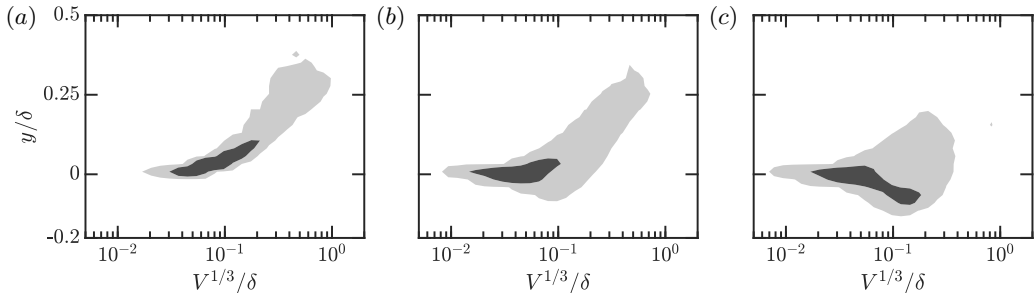


FIGURE 10. Probability density function of the centroid distribution for interfacial eddies, for canopies (a) $I_{S36 \times 36}$ (dense); (b) $I_{S72 \times 72}$ (intermediate); and (c) $I_{S432 \times 432}$ (sparse). The shaded contours enclose 95% and 50% of the eddies, respectively.

9(b, c) for canopy $I_{S216 \times 216}$, for which they elongate up to $x_{50,vol}^+ \approx x_{50,uv}^+ \approx 0.8\delta^+ \approx 440$ in the streamwise direction and $z_{50,vol}^+ \approx z_{50,uv}^+ \approx 0.4\delta^+ \approx 220$ in the spanwise direction. The figure also shows that the eddy-size statistics based on either volume or $u'v'$ are very similar, indicating that either one can be used to characterise the location and topology of the interfacial eddies. For simplicity, we present results based on volume in the remainder of the paper.

The wall-normal distribution of the interfacial eddies varies significantly with canopy density, providing useful metrics to characterise the density regime. As shown in figure 10(a), a dense canopy like $I_{S36 \times 36}$ precludes the overlying eddies from penetrating into it. In this case, small structures reside near the tips, while the larger ones reside essentially above the tips, with fewer than 1% of the interfacial eddies having centroids below the tips. In contrast, a sparse canopy like $I_{S432 \times 432}$ allows vigorous penetration of turbulent eddies into the canopy, with approximately 60% of the interfacial eddies having centroids below the tips, as depicted in figure 10(c). An intermediate canopy like $I_{S72 \times 72}$ in figure 10(b) lies between the two limits, with about 30% of the interfacial eddies having centroids below the tips.

To further investigate the wall-normal distribution of eddy volume, we examine the streamwise and spanwise widths at each height of the interfacial eddies. Figure 11 illustrates the typical spanwise width of eddies $z_{50,vol}^+$ (hereafter simplified as z_{50}^+) for dense to sparse canopies, $I_{S36 \times 36}$, $I_{S72 \times 72}$ and $I_{S432 \times 432}$. As shown in figure 11(a), the interfacial eddies generally have a large span, up to $z_{50}^+ \approx 180$, compared to the element pitch in the dense canopy $I_{S36 \times 36}$, and few of these eddies can penetrate. However, the intermediate canopy $I_{S72 \times 72}$ in figure 11(b) allows larger eddies, with widths comparable to its pitch, $z_{50}^+ \approx s_z^+ \approx 72$, to partially penetrate into the canopy, while the narrower eddies, with $z_{50}^+ \ll s_z^+$, penetrate more effectively and can reach the floor. The influence of different canopy parameters, including s_z^+ , on turbulence penetration will be further discussed in §4. As shown in figure 11(c), for a sparse canopy like $I_{S432 \times 432}$, turbulence penetrates relatively unhindered, easily reaching the floor. Even deep within this sparse canopy, the characteristic eddy width remains comparable to its footprint at the tips. In figures 11(a-c), lower contour levels tend to capture the large-eddy tails within the probability distribution function, especially above the dense canopy and within the sparse canopy. In these regions with minimal obstruction, where the eddies are not constrained by the presence of canopy elements, turbulence spans a broader range of eddy sizes. Consequently, including a larger portion of eddies, by using a lower contour level, increases the contribution of the large but infrequent eddies. We also show that as long as the n th percentile captures the majority of the volume for each

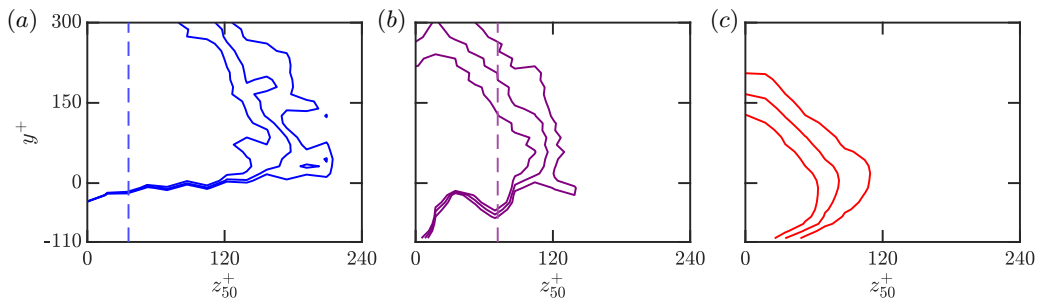


FIGURE 11. Probability density function of the characteristic spanwise width of interfacial eddies for canopies (a) $IS_{36 \times 36}$ (dense); (b) $IS_{72 \times 72}$ (intermediate); and (c) $IS_{432 \times 432}$ (sparse). The contours enclose 80%, 75% and 70% eddies. The dashed lines mark the corresponding element pitch $s_z^+ \approx 36, 72$, and 432 (the latter is beyond the abscissa range displayed).

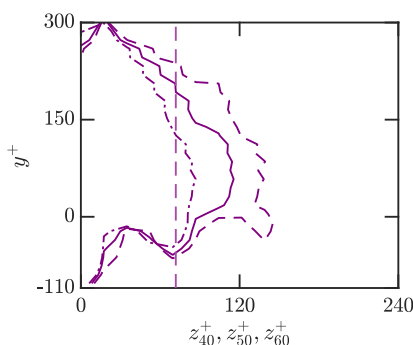


FIGURE 12. Probability density function of the spanwise width of interfacial eddies for canopy $IS_{72 \times 72}$. The dash-dotted, solid and dashed contours represent z_{40}^+ , z_{50}^+ and z_{60}^+ , respectively; the vertical dashed line mark the element pitch $s_z^+ \approx 72$. The contours enclose 75% of the eddies.

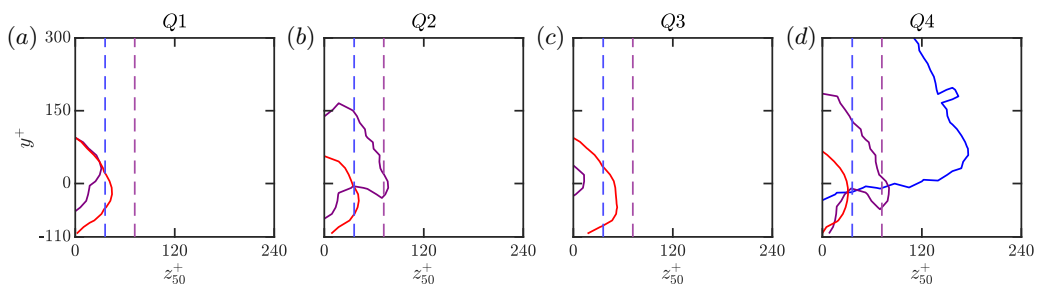


FIGURE 13. Probability density function of the spanwise width of interfacial eddies from different $u'v'$ quadrants for canopies (a) $IS_{36 \times 36}$ (dense); (b) $IS_{72 \times 72}$ (intermediate); and (c) $IS_{432 \times 432}$ (sparse). The contour level encloses 75% of the eddies. The colour scheme is as in figure 11.

eddy, the characteristic width within the canopy is essentially insensitive to the choice of percentile. For instance, figure 12 shows that spanwise widths z_{40}^+ , z_{50}^+ and z_{60}^+ are similar within the canopy, and differ only above it. For simplicity, the discussion in §4 presents the characteristic width of eddies using x_{50}^+ and z_{50}^+ , with a contour level that encloses 75% of the eddies within the probability density function.

In addition to exploring the structures overall, we can also analyse separately the characteristics of structures in different $u'v'$ quadrants (Lozano-Durán & Jiménez 2014). Figure 13 depicts the typical width of eddies across all four quadrants, using the same

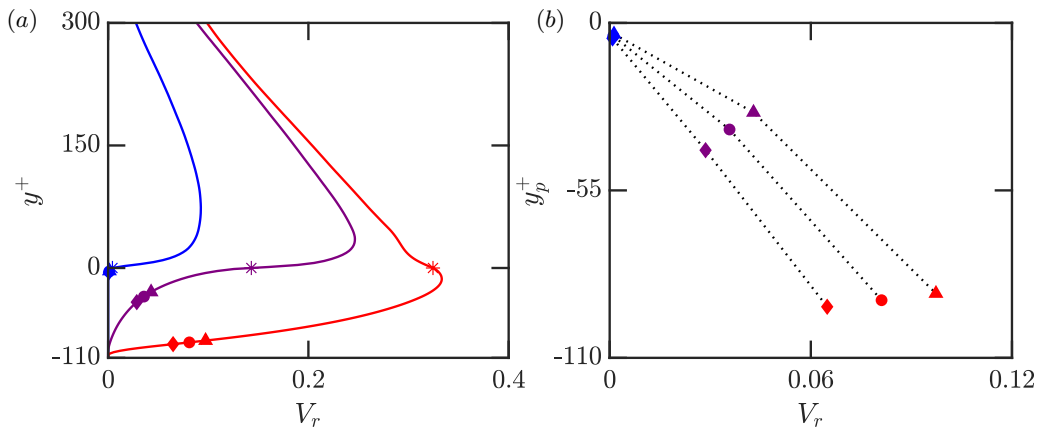


FIGURE 14. Relative volume V_r occupied by interfacial eddies at each height. The colour scheme is as in figure 11. Symbols *, ▲, ● and ◆ indicate the height where $V_r/V_{r,tip} = 1.0, 0.3, 0.25$, and 0.2 , respectively. In (b), the black dashed lines connect markers with the same value of $V_r/V_{r,tip}$ across different canopies.

contour level as in figure 11. This analysis provides insights into how structures from different quadrants, e.g. sweeps and ejections, penetrate differently. For the dense canopy $IS_{36 \times 36}$, sweeps dominate the turbulent structures. This is expected because the stress balance in a turbulent channel requires $\overline{u'v'} < 0$, which enhances the significance of sweeps and ejections with $u'v' < 0$. Furthermore, near the canopy-tip plane, ejections and outward interactions with $v' > 0$ are significantly hindered by the canopy drag (Huang *et al.* 2009; Sharma & García-Mayoral 2020b). As a result, only large sweeping structures are observed to penetrate slightly into the dense canopy with very few ejections springing out of it. For the intermediate canopy, sweeps and ejections exhibit larger spanwise widths and occur more frequently than inward and outward interactions. This observation is consistent with previous studies by Gardiner (1994), Novak *et al.* (2000), and Dupont *et al.* (2010), who reported the dominance of sweeps and ejections within and above vegetation canopies. In addition, these studies noted that sweeps generally contribute more significantly to Reynolds shear stress compared to ejections. For a sparse canopy like $IS_{432 \times 432}$, structures from different quadrants exhibit similar spanwise widths and occur with comparable frequency, suggesting a more uniform contribution from all four quadrants.

Besides the typical location and size of structures, we are interested in quantifying penetration depth. We do so based on the relative planar volume V_r , defined as the fraction of the domain at each height occupied by the interfacial eddies (Del Alamo *et al.* 2006). For a sparse canopy like $IS_{432 \times 432}$, where turbulence can freely penetrate within, figure 14(a) shows that V_r decays slowly with depth into the canopy, remaining comparable to its footprint at the tips, $V_{r,tip}$, even deep within the canopy. For an intermediate canopy such as $IS_{72 \times 572}$, where turbulence penetration is partially obstructed, V_r decays more rapidly. For a dense canopy like $IS_{36 \times 36}$, eddies are essentially precluded from entering the canopy, and V_r vanishes immediately below the tips. Based on these observations, we define the ‘penetration depth’ y_p^+ as the depth at which V_r becomes small relative to its footprint at the tips. The sensitivity analysis in figure 14(b) demonstrates that for $V_r/V_{r,tip} = 0.2-0.3$, y_p^+ is essentially insensitive to the chosen threshold. Dense canopies consistently result in minimal penetration, with $y_p^+ \approx 0$, while sparse canopies have penetration depths comparable to their height, $y_p^+ \approx -h^+$. We thus use the threshold

$V_r/V_{r,tip} = 0.25$ to determine y_p^+ from here on. This single-point indicator quantifies the depth of turbulence penetration and enables a simple comparative analysis across different canopies.

4. Results and discussion

With the metrics to quantify the extent and depth of turbulence penetration proposed above, we now apply them to our DNSs, examining the influence of one canopy parameter at a time. In §4.1, we first explore the effect of canopy layout by making the elements closely packed in either the streamwise or spanwise direction while keeping frontal density λ_f constant. This allows us to demonstrate that the same value of λ_f does not necessarily correspond to the same density regime, as advanced in §1. In §4.2, we vary the pitch between elements in either the spanwise or streamwise direction to identify in which direction variations have a greater influence on turbulence penetration. In §4.3, we vary either the element pitch or gap for isotropic canopies to determine which of the two has the most influence. In §4.4, we investigate the same canopy at different Reynolds numbers to determine the length scale governing turbulence penetration. Finally, in §4.5, we put together all the preceding results to propose a single parameter to encapsulate canopy density.

4.1. Different density regimes for the same frontal density λ_f

In this subsection, we demonstrate that frontal density λ_f alone cannot fully characterise the density for canopies with an anisotropic layout. Figure 3 illustrated that for canopies with the same number of elements per unit area and identical λ_f , the arrangement of elements can significantly influence how much blockage they produce on the overlying eddies, affecting the degree of turbulence penetration. This difference in penetration can now be quantified with the metrics proposed in §3.

Figure 15 depicts the typical location and size of the penetrating eddies for both isotropic and anisotropic canopies. As shown in figure 15(a), canopy $I_{S36 \times 36}$, with the highest density value of $\lambda_f \approx 2.04$, behaves as dense, as less than 1% of the eddies have centroids below the canopy-tip plane. As the elements are spaced further apart, canopies $I_{S54 \times 54}$ and $I_{S72 \times 72}$ allow eddies to penetrate moderately into the canopy. For these two intermediate canopies, eddies of size $V^{1/3} \gtrsim 0.05 \delta$ can extend well above and below the tips, and more than 20% eddies have centroids below the tips. For canopies $I_{S108 \times 108}$ to $I_{S432 \times 432}$, with pitch $s^+ > 100$ and $\lambda_f \approx 0.23$ -0.01, turbulence penetrates with little obstruction, with more than 60% of the eddies having centroids below the tips. Sharma & García-Mayoral (2020a) performed DNSs for isotropic layouts of filaments, and argued that canopies were sparse if the pitch between elements was $s^+ > 100$, which allowed sufficient space for near-wall streaks to fit within. However, while λ_f captures the overall trends of turbulence penetration in dense and intermediate canopies, it fails to distinguish the sparser canopies $I_{S108 \times 108}$ to $I_{S432 \times 432}$ in figure 15(a), which essentially have similar distributions of centroids. More importantly, figures 15(b-f) illustrate that the same value of λ_f does not necessarily result in the same density regime. For instance, canopies with $\lambda_f \approx 0.91$ would typically be classified as dense based on λ_f alone (Nepf 2012a; Brunet 2020). However, as shown in figure 15(b), although the isotropic and the fence-like canopies $I_{S54 \times 54}$ and $F_{S108 \times 27}$ behave as dense, the canyon-like canopy $C_{S27 \times 108}$, with the same λ_f , behaves as sparse, with approximately 65% of the interfacial eddies having centroids below the tips. At lower densities, the isotropic and fence-like canopies allow eddies to penetrate more effectively, see figures 15(c-e), while canyon-like canopies consistently result in the most significant turbulent penetration for a given λ_f . Eventually,

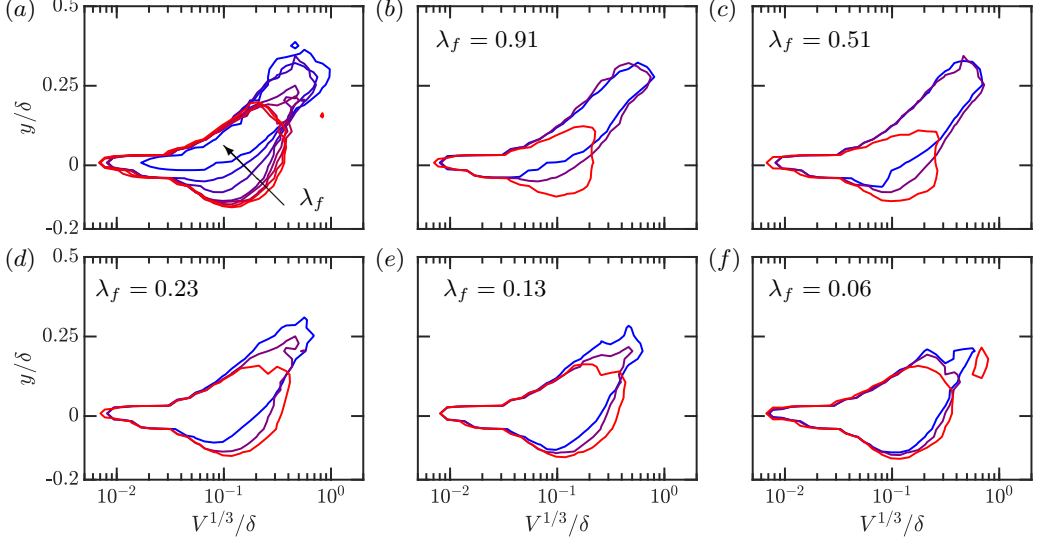


FIGURE 15. Probability density function of the spatial distribution of interfacial eddies. (a), isotropic-layout canopies with increasing frontal density $\lambda_f \approx 0.01$ -2.04 from red to blue. (b) through (f), decreasing frontal density $\lambda_f \approx 0.91$ -0.06; blue, magenta and red indicate fence-like, isotropic and canyon-like canopies, respectively, with the same λ_f . The contours enclose 75% of the eddies.

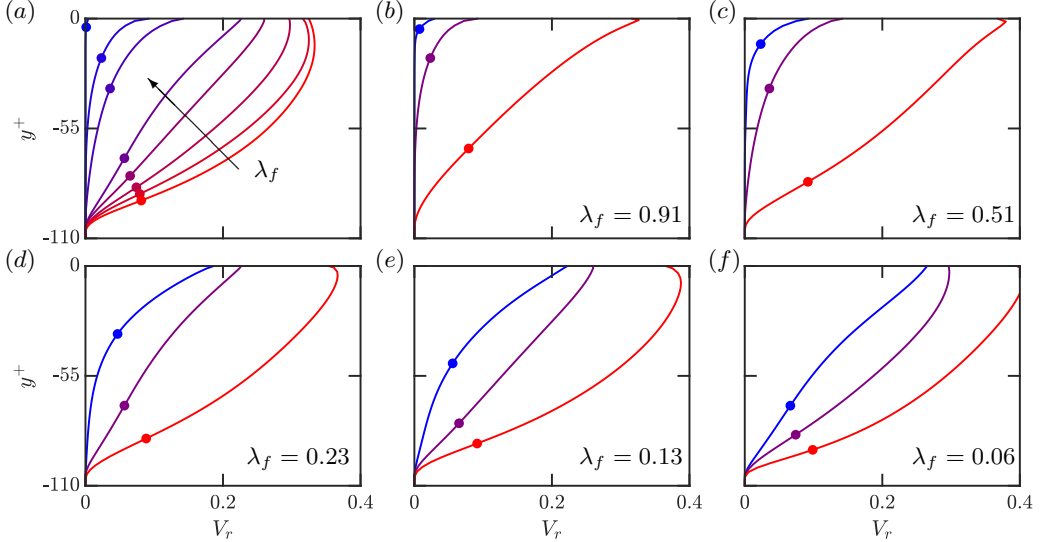


FIGURE 16. Relative volume V_r occupied by interfacial eddies at each height. Markers • indicate the penetration depth y_p^+ where $V_r/V_{r,tip} = 0.25$. The canopies portrayed in each panel and the colour scheme are the same as in the respective panels in figure 15.

for low enough frontal densities $\lambda_f \lesssim 0.06$, turbulence can enter freely into the canopies regardless of the canyon, fence or isotropic layout.

In addition to examining the distribution of centroids, we also analyse the penetration depth y_p^+ of eddies below the canopy-tip plane, as portrayed in figure 16. In agreement with figure 15(a), figure 16(a) illustrates that turbulence only penetrates moderately into the dense to intermediate canopies $\text{IS}_{36 \times 36}$ to $\text{IS}_{72 \times 72}$, with $y_p^+ \gtrsim 35$. In contrast,

turbulence penetrates significantly deeper into the sparser canopies $I_{S108 \times 108}$ to $I_{S432 \times 432}$, where $y_p^+ \approx 70$ -91. Figures 16(b-f) show that the influence of element layout is more noticeable for canopies with a higher value of frontal density $\lambda_f \gtrsim 0.51$, where the isotropic and the fence-like layouts induce more blockage on the overlying eddies compared to the canyon-like layout. However, once the frontal density is small, $\lambda_f \lesssim 0.06$, the canopy behaves as sparse regardless of its layout anisotropy, suggesting that λ_f provides only a notional measure of density for denser canopies. As depicted in figures 16(b,c), the isotropic and the fence-like canopies essentially preclude the eddies from entering the canopy, whereas the canyon-like canopy allows effective turbulence penetration, with $y_p^+ \approx 65$ even at $\lambda_f \approx 0.91$. As λ_f decreases, the isotropic and the fence-like canopies in figures 16(d,e) allow turbulence to penetrate within, but they consistently behave as denser compared to the corresponding canyon-like canopies. In the sparse limit, $\lambda_f \lesssim 0.06$, turbulence penetrates freely into the canopy, regardless of the layout. We also note that the canyon-like canopies in figures 16(b-f) appear as sparse for all λ_f considered, with $y_p^+ \gtrsim 65$ -92. The observations in figures 15 and 16 suggest that the depth of turbulence penetration has a dependence on whether the canopy elements are closely packed in the streamwise or spanwise direction, with the former behaving as sparser. In §4.2 and §4.3, we will further examine the effects of element pitch and gap in different directions.

4.2. Influence of streamwise and spanwise pitch

We have shown that, for a fixed λ_f , the location of interfacial eddies and their penetration depth depend on whether the canopy elements are more closely packed in the streamwise or spanwise direction. To further investigate the effect of the streamwise and spanwise arrangement, we now vary the element pitch separately in the streamwise or spanwise direction while keeping the element geometry fixed. This allows us to examine the effects of s_x^+ and s_z^+ independently, and to better understand how canopy anisotropy affects turbulence penetration.

Figure 17 depicts the characteristic streamwise width x_{50}^+ and spanwise width z_{50}^+ of structures in different quadrants. Figures 17(a-d) show that canopies with a fixed spanwise pitch $s_z^+ \approx 108$ allow turbulence to penetrate effectively into the canopy, and the eddies within can elongate up to $x_{50}^+ \approx 120$, with no significant influence of the value of s_x^+ . However, in contrast to these fixed- s_z canopies, where turbulence penetration is largely unimpeded, canopies with a constant streamwise pitch $s_x^+ \approx 108$ exhibit different penetration behaviours depending on their spanwise pitch, as illustrated in figures 17(e-h). A fence-like canopy such as $X_{S108 \times 27}$ significantly restricts turbulence penetration, allowing limited Q2 and Q4 structures to penetrate, with Q4 structures having the highest occurrence and the largest width, up to $z_{50}^+ \approx 100$. This suggests that sweeps dominate turbulence penetration within fence-like canopies, which is consistent with previous observations on obstructing vegetation canopies (Poggi *et al.* 2004; Yue *et al.* 2007; Bailey & Stoll 2013). Bailey & Stoll (2013) reported that the dominance of sweeps persists even when the streamwise pitch between the fences increases to $s_x/h \approx 3$. In contrast, as s_z^+ increases, canopies such as $X_{S108 \times 108}$ and $X_{S108 \times 216}$ allow turbulence to penetrate more effectively, and structures in different quadrants have a more uniform contribution to turbulence penetration. The correlation between turbulence penetration and spanwise pitch is not surprising; as turbulence is advected downstream, eddies will be obstructed by the elements they encounter. In turn, when the elements are spaced further apart in the spanwise direction, once eddies have penetrated within the canopy they will travel through the canyons without encountering any significant obstruction.

In agreement with figure 17, figure 18(a) illustrates that all the canopies with large

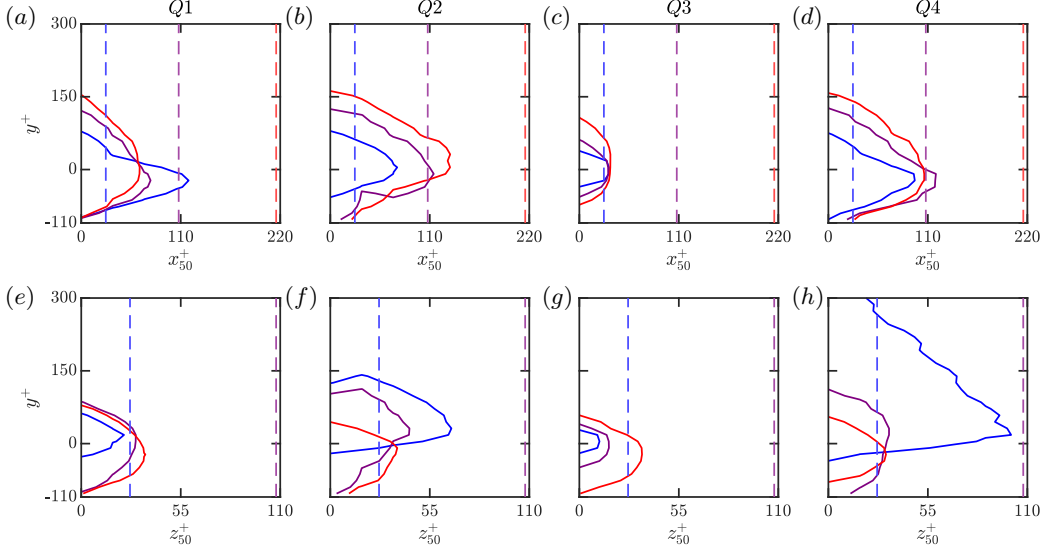


FIGURE 17. Probability density function of the characteristic wall-parallel sizes of interfacial eddies from different quadrants. (a-d), eddy streamwise length for canopies with a fixed $s_z^+ \approx 108$; (e-h), eddy spanwise width for canopies with a fixed $s_x^+ \approx 108$. The contours from blue to red are for canopies with decreasing frontal densities $\lambda_f \approx 0.91$ -0.11; the dashed lines mark the canopy streamwise and spanwise pitch, $s_x^+, s_z^+ \approx 27, 108$, and 216. The contours enclose 75% overall eddies.

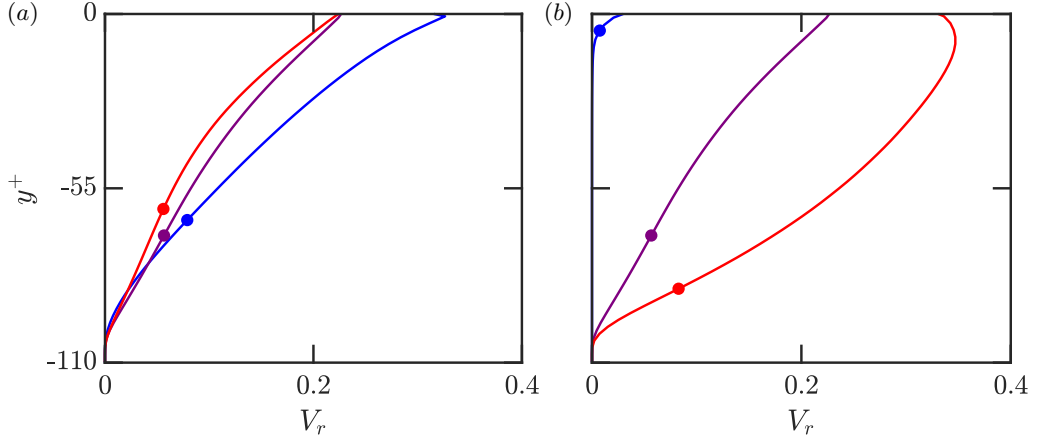


FIGURE 18. Relative volume V_r occupied at each height by interfacial eddies: canopies with (a) fixed $s_z^+ \approx 108$ and (b) fixed $s_x^+ \approx 108$. Markers • indicate the penetration depth y_p^+ where $V_r/V_{r,tip} = 0.25$. The colour scheme is as that in figure 17, from blue to red canopies with decreasing frontal densities $\lambda_f \approx 0.91$ -0.11.

spanwise pitch $s_z^+ \approx 108$ behave as sparse, regardless of their frontal density $\lambda_f \approx 0.11$ -0.91, allowing eddies to effectively penetrate into the canopy with a penetration depth of $y_p^+ \approx 65$. In contrast, figure 18(b) highlights that when the pitch in x is fixed to $s_x^+ \approx 108$, the canopies behave as increasingly sparser as the spanwise pitch increases from $s_z^+ \approx 27$ to $s_z^+ \approx 108$. This transition in density regime is marked by a substantial increase in penetration depth, from $y_p^+ \approx 5$ for the dense canopy $X_{S108 \times 27}$ to $y_p^+ \approx 87$ for the sparse canopy $X_{S108 \times 216}$.

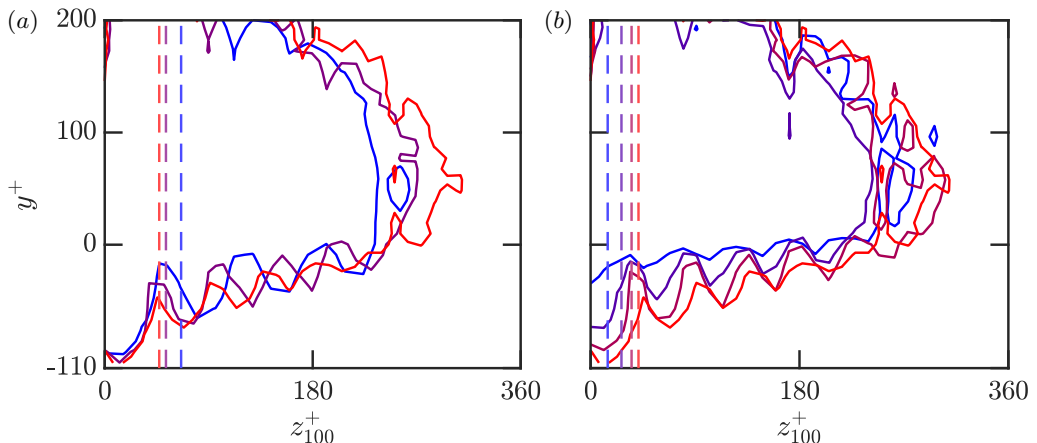


FIGURE 19. Probability density function of the total spanwise width of interfacial eddies, $z_{100}^+ = z_{max}^+ - z_{min}^+$, for canopies with (a) fixed gap $g_z^+ \approx 41$ and (b) fixed pitch $s_z^+ \approx 47$. The contours from blue to red represent canopies with decreasing frontal densities, $\lambda_f \approx 0.63$ -0.29 in (a) and $\lambda_f \approx 1.61$ -0.29 in (b); the dashed lines mark the pitch $s_z^+ \approx 66, 53, 47$ in (a) and the gap $g_z^+ \approx 15, 267, 35, 41$ in (b). The contours enclose 75% of the interfacial eddies.

4.3. Influence of element pitch versus gap width

We have shown that as the canopy elements are spaced further apart in the spanwise direction, the canopy transitions to a sparser regime, whereas variations in the streamwise direction have little impact on the density regime. However, it remains to be determined whether this difference in turbulence penetration is due to the increase in gap or in pitch. We address this question by examining canopies with either a fixed inter-element gap and varying element pitch or a fixed pitch and varying gap.

Figure 19 depicts the total spanwise width of interfacial eddies, $z_{100}^+ = z_{max}^+ - z_{min}^+$, to illustrate how the pitch s_z^+ and gap g_z^+ influence the ‘accessible space’ that penetrating eddies must fit within. As shown in panel (a), within the canopies with a fixed gap $g_z^+ \approx 41$, the distribution of z_{100}^+ remains largely similar, regardless of the variations in s_z^+ . In contrast, panel (b) shows that increasing g_z^+ while keeping s_z^+ constant enables eddies with larger widths to penetrate more easily into the canopy, suggesting that gap width, rather than pitch, determines the ‘accessibility’ of the canopy for turbulence penetration. For all canopies considered in figure 19, only eddies with widths smaller than the gap size, $z_{100}^+ < g_z^+$, can penetrate all the way into the canopy. When this gap is very small ($g_z^+ \lesssim 15$), not even the smallest turbulent structures, of size $\lambda^+ \sim \mathcal{O}(20)$ (Jiménez 2012; Jiménez 2013), can fit in between the elements, and thus turbulence penetration is essentially fully impeded, as evidenced by the results for canopy S47_{G14×14} in figure 19(b).

Figure 20 further illustrates the relative contributions from different quadrants to the overall turbulence penetration. For all canopies shown in figure 20, sweeps and ejections dominate the penetrating structures, and sweeps are generally more intense and penetrate deeper within the canopy compared to ejections. This observation aligns with the findings by Collineau & Brunet (1993), who investigated flows over an obstructing pine forest and found that the ratio of the total stress fraction transferred by sweeps to that transferred by ejections is up to 2-3 at height $y/h \approx 0.8$. The dominance of sweeps has also been reported on other obstructing vegetation canopies (Novak *et al.* 2000; Dupont *et al.* 2011; Dupont & Patton 2012), as summarised in Brunet (2020). Figures 20(d,h) show that large sweep-type eddies with width $z_{100}^+ > g_z^+$ cannot fully enter the canopy, but

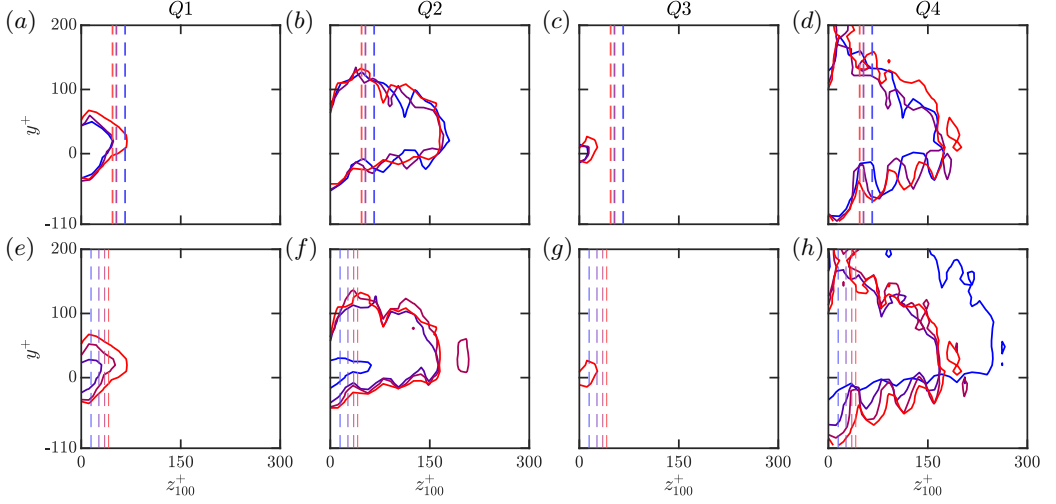


FIGURE 20. Probability density function of the total spanwise width of eddies from different $u'v'$ quadrants, for canopies with (a-d) fixed gap $g_z^+ \approx 41$ and (e-h) fixed pitch $s_z^+ \approx 47$. Colours and contour levels are as in figure 19.

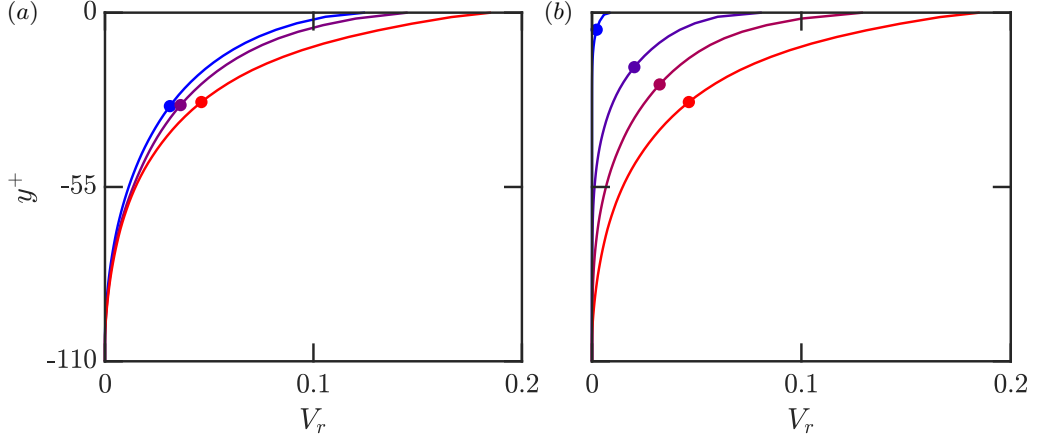


FIGURE 21. Relative volume V_r occupied at each height by interfacial eddies. Canopies with (a) fixed gap $g_z^+ \approx 41$ and (b) fixed pitch $s_z^+ \approx 47$. Markers \bullet indicate the penetration depth y_p^+ where $V_r/V_{r,tip} = 0.25$. The colour scheme is as in figure 19.

their ‘feet’ may partially penetrate if they fit within the gap between elements. As an example, for canopy $S47_{G41 \times 41}$ in figure 20(h), for large eddies that span multiple canopy elements, their width z_{100}^+ exhibits harmonics of the element pitch $s_z^+ \approx 47$ within the canopy. Eddies with increasing widths $z_{100}^+ \approx 70, 115, 160$ have decreasing penetration depths $y^+ \approx 75, 60, 40$, respectively, demonstrating a reduced penetration depth for larger footprints.

In agreement with figures 19 and 20, figure 21 illustrates the dependence of the penetration depth on the spanwise gap between elements. As shown in figure 21(a), the penetration depth remains similar for cases with fixed gap size, $y_p^+ \approx 30$, independently of variations in pitch. However, figure 21(b) demonstrates that canopies behave as sparser with increasing spanwise gap g_z^+ . As the spanwise gap widens from $g_z^+ \approx 15$ to $g_z^+ \approx 40$, the penetration depth increases from $y_p^+ \approx 5$ to $y_p^+ \approx 30$. The main contribution to the

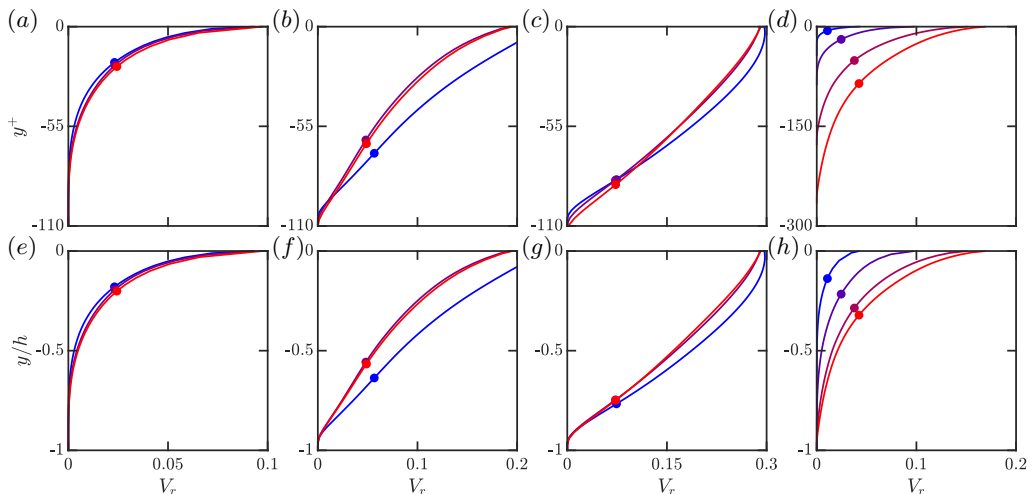


FIGURE 22. Relative volume V_r occupied at each height by interfacial eddies. (a, e), (b, f) and (c, g) are, respectively for $\lambda_f \approx 0.91$, 0.23 , and 0.06 , ‘inner-similar’ canopies with the same s^+ , g^+ and h^+ . (d, h) are ‘outer-similar’ canopies with $\lambda_f \approx 0.70$ and the same s/δ , g/δ and h/δ . Lines from blue to red indicate increasing Reynolds number $Re_\tau \approx 550$ – 2000 . Markers \bullet indicate the penetration depth y_p^+ where $V_r/V_{r,tip} = 0.25$.

net eddy volume within the canopies is from Q4 structures, which typically have a larger width within the canopy compared to those from the other quadrants, as demonstrated in figures 20(d, h).

4.4. Influence of the Reynolds number

We have so far argued that the penetration of the overlying turbulence depends on whether the span of canopy ‘canyons’ is sufficient for the interfacial turbulent eddies to fit within. This inherently involves not only the canopy dimensions, but also the characteristic dimensions of those eddies. Assuming that their dimensions are set by the overlying turbulent dynamics, classical scaling would imply that they scale in inner units if they are sufficiently embedded in the near-wall region, and with the height above a notional wall if they lie farther above and into the log layer. The governing parameter would be the zero-plane-displacement height, y_d^+ , the depth perceived as the origin by the overlying-turbulence eddies, which we have recently reported in detail for a wide range of canopy densities (Chen & García-Mayoral 2023). For most of the present cases, with low to moderate Reynolds numbers and $y_d^+ \lesssim 100$, we would expect interfacial eddies to scale in inner units. To investigate this, we examine canopies with either the same dimensions in inner units (same s^+ , g^+ and h^+) or in outer units (same s/δ , g/δ and h/δ), for different frontal densities λ_f and across different Reynolds numbers Re_τ .

Figure 22 depicts the decay rate of the eddy volume and the penetration depth for both the ‘inner-similar’ and the ‘outer-similar’ canopies from table 1. As shown in panels (a–c) and (e–g), when a canopy remains the same in inner units for varying Re_τ , be it dense as in panels (a, e), intermediate as in (b, f), or sparse as in (c, g), it exhibits similar turbulent penetration. This is consistent with the scaling of interfacial eddies in viscous units mentioned above. Scaling of the flow in inner units over canopies and rough surfaces has also been reported by Chan *et al.* (2015) and Sharma & García-Mayoral (2020a, b) at Re_τ and s^+ – h^+ values comparable to the present ones.

In contrast, a canopy that remains the same in outer units, i.e. with fixed s/h and g/h

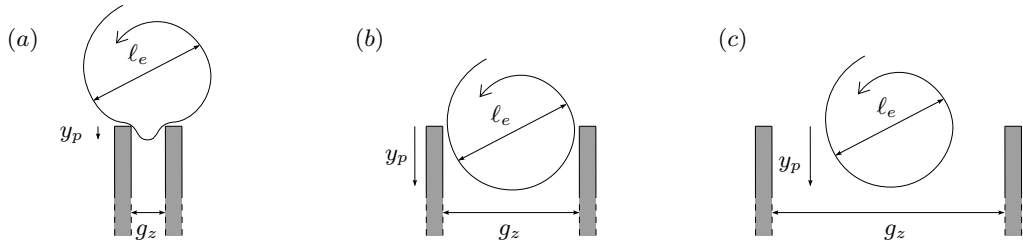


FIGURE 23. Sketch of the penetration depth y_p for interfacial eddies of size ℓ_e , depending on the value of ℓ_e relative to the spanwise gap between canopy elements, g_z . (a), $\ell_e > g_z$; (b), $\ell_e \sim g_z$; (c), $\ell_e < g_z$.

but varying g^+ and all other dimensions in viscous units, can exhibit different behaviours as Re_τ varies. This is portrayed for the canopy of OS180_{G15×15} in figures 22(d, h). This canopy behaves as dense at $Re_\tau \approx 180$, for which $y_p^+ \approx 5$ and the turbulence essentially skims above, with limited penetration. However, for increasing Reynolds numbers, the canopy behaves as increasingly sparser, as the penetration depth increases gradually to $y_p^+ \approx 85$ at $Re_\tau \approx 1080$, for which y_p^+ is of the order of the zero-plane displacement y_d^+ . The increase in y_p^+ is not linear with the canopy dimensions in inner units, e.g. with g_z^+ , which would result in a collapse of the results in panel 22(h). For $g_z^+ \approx 15$, eddy penetration is negligible, and only for $g_z^+ \gtrsim 30$ it begins to approach $y_p \approx g_z$ and an eventual collapse in panel (h). This is what one would expect if the impedance exerted by the canopy elements on the interfacial eddies was essentially viscous for $g_z^+ \approx 15$, but became increasingly inertial for $y_d^+ \approx 50$ -100; interfacial eddies would then scale with y_d , and the vanishing effect of viscosity would result in $y_d \sim y_p \sim g_z$. Finally, we note that the increase in penetration depth has been observed for a canopy with $y_p \approx 0.15h$ - $0.35h$, and would not occur for a sparse canopy with $y_p \approx h$, for which no further increase of y_p would be possible due to the presence of the flow. The conclusion is that canopies that are sparse at low Re_τ remain sparse as Re_τ increases, while dense ones can behave as increasingly sparse as the interfacial eddy size decreases relative to the canopy gap. We expect, however, that this effect eventually saturates, as the penetration depth asymptotes to $y_p \approx g_z$; verifying this will require measurements at Reynolds numbers higher than our current computational capability.

4.5. What makes a canopy dense or sparse?

The preceding discussion suggests that, depending on the ratio between canopy gap g_z and the width of interfacial eddies ℓ_e , the eddies will be in one of the situations sketched in figure 23. For closely packed elements, $g_z < \ell_e$, the eddies would not fit in the gaps, and their penetration would be limited as sketched in panel (a) – to a few viscous units if $g_z^+ \lesssim 15$ or to order $y_p \sim g_z$ otherwise. For a wider separation between elements, such that $g_z \sim \ell_e$ as in panel (b), eddies could penetrate into the canopy, but the depth of the penetration would be limited by their own size, as the span-to-height ratio of wall-turbulent eddies is of order unity (Flores & Jiménez 2010). We would then have $y_p \sim g_z$ once more. For widely separated elements, $g_z > \ell_e$ as in panel (c), interfacial eddies could traverse the plane of the tips freely and penetrate into the canopy undisturbed, but the penetration depth would again be limited by the eddy size itself, yielding $y_p \sim \ell_e < g_z$. The latter case is only possible if the zero-plane displacement y_d , which sets the scale for the eddy size ℓ_e , is small enough to result in $\ell_e < g_z$. This in turn is only possible if y_d is restricted by the proximity of the floor, rather than by g_z , that is, for sparse canopies with $y_p \approx h$.

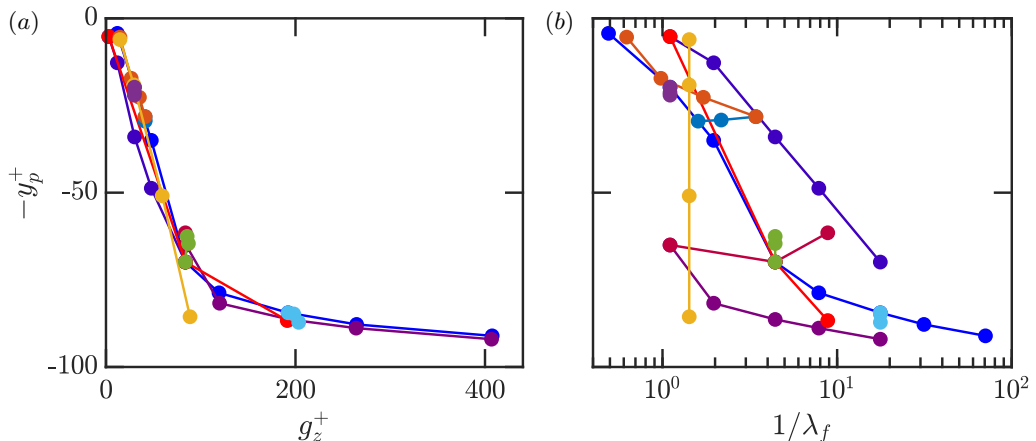


FIGURE 24. Penetration depth y_p^+ versus (a) spanwise gap g_z^+ and (b) frontal density λ_f . \bullet , isotropic-layout canopies; \bullet , ‘fence-like’ canopies; \bullet , ‘canyon-like’ canopies; \bullet , fixed- s_z canopies; \bullet , fixed- s_x canopies; \bullet , fixed-gap canopies; \bullet , fixed-pitch canopies; \bullet , ‘outer-similar’ canopies; \bullet , ‘inner-similar’ canopies with $\lambda_f \approx 0.91$; \bullet , ‘inner-similar’ canopies with $\lambda_f \approx 0.23$; \bullet , ‘inner-similar’ canopies with $\lambda_f \approx 0.11$.

Given the limited Re_τ in our simulations, we first assume that across our canopies the interfacial-eddy size broadly scales in viscous units. If that is the case, g_z^+ would be a reasonable surrogate for the ratio g_z/ℓ_e , and can therefore be used to characterise eddy penetration. This is illustrated in figure 24, which shows that g_z^+ is a good predictor for y_p^+ and significantly outperforms the classic frontal density λ_f . Starting at small g_z^+ , the penetration depth y_p^+ increases monotonically with g_z^+ until it eventually becomes comparable to the canopy height, $h^+ \approx 100$ for most of our canopies. The only exception are the ‘outer-similar’ canopies discussed in §4.4, which have $h^+ \approx 50$ -270 and for which the last case has $y_p^+ \approx 85$, still far from the full canopy height $h^+ \approx 270$. This case appears as a slight outlier in figure 24(a).

The question that arises then is if, for our sparse canopies with eddy penetration essentially all the way to the floor, that penetration is restricted by the presence of the floor, or if it is already as much as it would be if the floor was further below. To address this, we have run three additional simulations for a dense, an intermediate and a sparse canopy in which we doubled the canopy height. The parameters of the simulations are summarised in table 2, which also includes the original simulations for reference. The results for y_p^+ are shown in figure 25(a). For dense and intermediate canopies, doubling the canopy height from $h^+ \approx 110$ to $h^+ \approx 220$ results in no significant change in the penetration depth y_p^+ , which remains essentially $y_p \approx g_z$. This is consistent with the representations for eddy penetration in figures 23(a-b). For the sparse canopy, however, doubling the canopy height results in an increase in y_p^+ , and an approach to the $y_p \approx g_z$ trend of denser canopies. This would correspond to a transition from the representation of figure 23(c) to the one in figure 23(b), and illustrates a secondary role of canopy height in the penetration of the overlying turbulence. We have so far considered the penetration of interfacial eddies as driven essentially by the dynamics and canopy properties at the interface with the overlying flow. For sparse canopies with $y_p \approx h$, however, increasing their height can have a direct result of increasing the depth of the zero-plane displacement. This, in turn, results in an increase of the typical size of interfacial eddies, and thus of their penetration depth, $y_p \sim \ell_e$, which can continue until they reach $\ell_e \approx g_z$, when the penetration depth begins to be limited by the canopy canyon width.

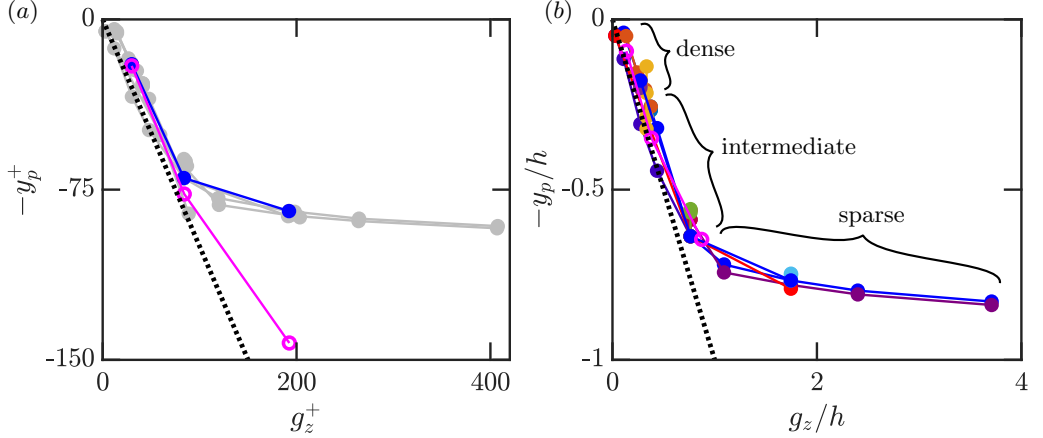


FIGURE 25. Penetration depth versus spanwise gap, scaled (a) in viscous units as in figure 24(a), and (b) with the canopy height h . • and ◯, cases ‘I’ and ‘H220’ from table 2, respectively. In (a), ◉ is used for cases already portrayed in figure 24. In (b), colours are as in figure 24. The dotted lines are $y_p = g_z$.



	Case	$N_x \times N_z$	Re_τ	λ_f	g_z^+	g_x^+	s_z^+	s_x^+	h^+
Different height 	I _{S54×54}	64×32	549.7	0.91	30.0	30.0	54.0	54.0	109.9
	I _{S108×108}	32×16	548.7	0.23	83.8	83.8	107.7	107.7	109.7
	I _{S216×216}	16×8	550.7	0.06	192.2	192.2	216.3	216.3	110.1
	H220 _{S54×54}	64×32	549.2	1.81	30.0	30.0	53.9	53.9	219.7
	H220 _{S108×108}	32×16	550.9	0.45	84.1	84.1	108.2	108.2	220.4
	H220 _{S216×216}	16×8	551.6	0.11	192.6	192.6	216.6	216.6	220.7

TABLE 2. Simulation parameters for canopies with height doubled to $h^+ \approx 220$. The corresponding simulations with $h^+ \approx 110$ from table 1 are also included for reference.

Ultimately, canopy density can be characterised by what proportion of the canopy the overlying turbulence can penetrate, that is, by y_p/h . From the above discussion, we expect y_p/h to be roughly proportional to g_z/h for dense and intermediate canopies, and to approach $y_p/h \approx 1$ for sparse ones. This suggests that density can be characterised in a graph of y_p/h vs. g_z/h , as portrayed in figure 25(b). The figure is similar to figure 24(a), but the largest ‘outer-similar’ case, as well as the simulations with doubled height of figure 25(a), no longer appear as outliers, and collapse with the rest. The figure shows that canopies lie along the line $y_p/h = g_z/h$ for $g_z/h \lesssim 0.5$, and tend to a constant $y_p/h \approx 0.9$ for $g_z/h \gtrsim 1$. Dense canopies would be those with small penetration depth relative to the canopy height, e.g. $y_p/h \lesssim 0.2$, sparse ones those substantial penetration, e.g. $y_p/h \gtrsim 0.7$, and those in-between would have intermediate density and connect the two aforementioned limit trends, but mostly lying near the $y_p/h = g_z/h$ asymptote. In terms of gap-to-height ratio, dense canopies would have $g_z/h \lesssim 0.2$, intermediate ones $0.2 \lesssim g_z/h \lesssim 1$, and sparse ones $g_z/h \gtrsim 1$.

5. Conclusions

In the present work, we have identified and characterised canopy density regimes based on the penetration of eddies from the overlying turbulence. In the sparse regime,

turbulence penetrates with little obstruction into the canopy all the way to the canopy floor, whereas in the dense regime, this penetration is limited. We have examined the conventional measure of canopy density using frontal density λ_f , and found that λ_f alone cannot fully characterise canopy density, as it cannot capture e.g. the effect of different streamwise and spanwise spacing of the canopy elements or of the Reynolds number.

To measure turbulence penetration, we focus on flow structures of intense local Reynolds shear stress $u'v'$, as these structures are responsible for momentum transport and turbulence diffusion. We separate overlying-turbulence structures from texture-coherent ones by spectral filtering, and choose a suitable $u'v'$ threshold to delimit them through a percolation analysis. We then focus on the structures that are, at least partially, in the immediate vicinity of the canopy-tip plane, referring to them as ‘interfacial eddies’, and propose metrics to quantify their location, span and volume. We apply these metrics to analyse a series of canopies across a range of frontal densities $\lambda_f \approx 0.01$ -2.04, heights $h^+ \approx 44 - 266$, and Reynolds numbers $Re_\tau \approx 180 - 2000$.

Our results show that, for the same λ_f , streamwise-packed canopies with large spanwise gaps allow eddies to penetrate effectively, and thus behave as sparser compared to the corresponding isotropic and spanwise-packed canopies, which limit eddy penetration to a significantly greater degree. Streamwise-packed canopies with frontal densities as high as $\lambda_f \approx 0.9$ still behave as sparse, while only in the limit of very small frontal density, $\lambda_f \lesssim 0.06$, do canopies behave as sparse regardless of their anisotropy. Our results further show that turbulence penetration remains similar when the spanwise gap between canopy elements is fixed, regardless of their pitch and thickness. For closely packed canopies with small spanwise gaps, $g_z^+ \lesssim 15$, turbulence penetration is restricted to a few viscous units. As the spanwise gaps widen, canopies behave as increasingly sparse, allowing eddies to penetrate deeper and more vigorously. Turbulence penetration does not only depend on the canopy topology, but also on the Reynolds number. A canopy with fixed geometry can inhibit turbulence penetration at low Reynolds numbers, $Re_\tau \approx 180$, when its dimensions in viscous units, mainly g_z^+ , are small, but permit increasing penetration as Re_τ and g_z^+ increase. In turn, canopies with the same dimensions in inner units exhibit similar density regimes and penetration depth across different Re_τ .

Overall, our results suggest that turbulence penetration depends essentially on the spanwise gap between canopy elements, and how it compares to the typical spanwise size of interfacial eddies. The latter scales generally with the zero-plane displacement depth, resulting in a penetration depth $y_p \sim g_z$ unless further limited by the immediate vicinity of the canopy bed – something that occurs for sparse canopies. This leads to a characterisation of canopy density in terms of y_p/h , the proportion of the canopy that the overlying turbulence can penetrate, as a function of the canyon-width-to-element-height ratio g_z/h . Dense canopies have $g_z/h \lesssim 0.2$, their turbulence penetration is small and follows roughly $y_p \approx g_z$. Intermediate canopies have $0.2 \lesssim g_z/h \lesssim 1$, and experience an eventual departure from $y_p \approx g_z$ for large g_z/h . Sparse canopies have $g_z/h \gtrsim 1$, and their turbulence penetration approaches the full height of the canopy, $y_p/h \approx 0.9$.

Funding. This work was supported in part by the UK Engineering and Physical Sciences Research Council (EPSRC) under grant EP/S013083/1. Computational resources were provided by the University of Cambridge Research Computing Service under EPSRC Tier-2 grant EP/P020259/1 (project cs155), and by the UK ‘ARCHER2’ system under PRACE project pr1u1702 and EPSRC Access to HPC projects e776 and e800. For the purpose of open access, the authors have applied a Creative Commons Attribution (CC BY) licence to any Author Accepted Manuscript version arising from this submission.

Declaration of interests. The authors report no conflict of interest.

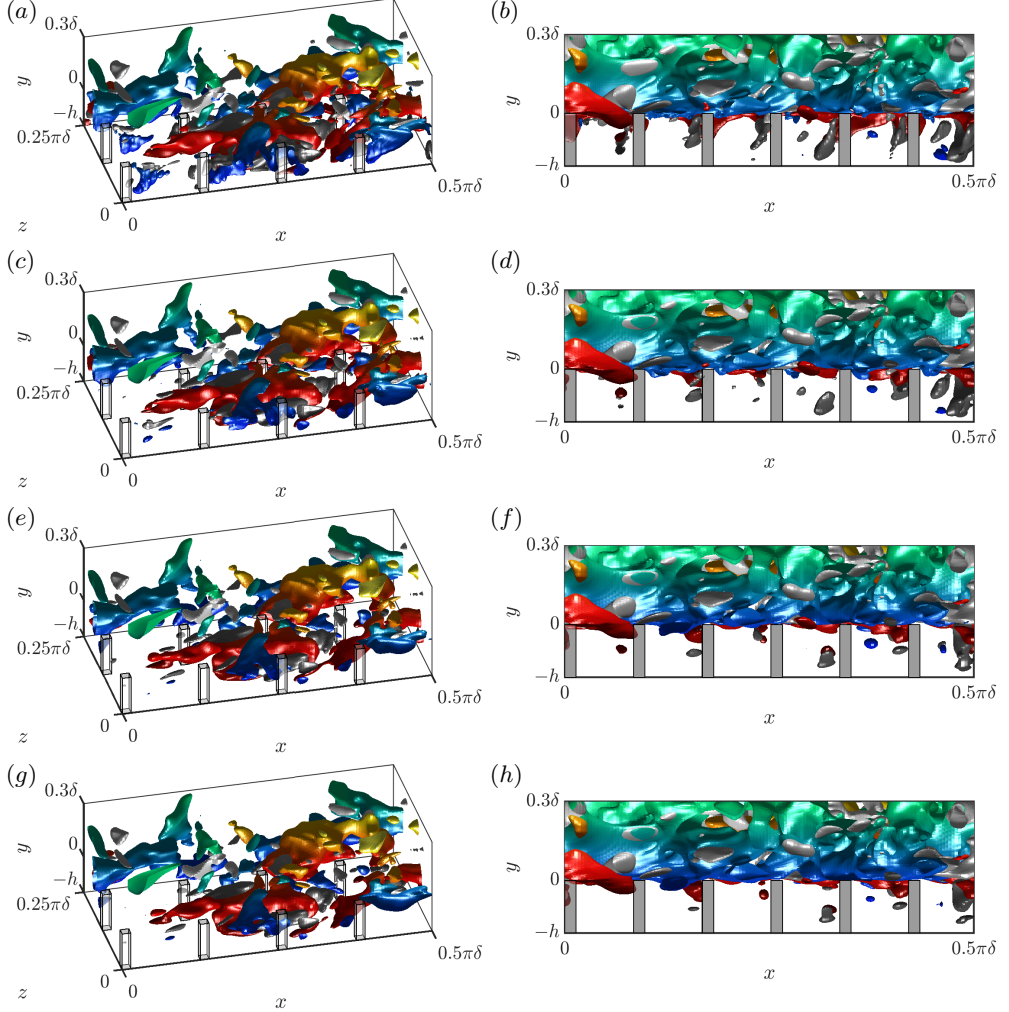


FIGURE 26. Instantaneous realisations of $u'v'$ structures for canopies $\text{IS}_{216 \times 216}$ (a, c, e, g) and $\text{FS}_{144 \times 36}$ (b, d, f, h). The filter levels are 100% (no filter) in (a, b), 99% in (c, d), 97% in (e, f) and 95% in (g, h). The structures are coloured by distance to the floor, ejections blue to green, sweeps red to yellow, and outward and inward interactions grey to white.

Appendix A. Sensitivity analysis for the filter of the element-coherent flow

In §3.1, we applied a spectral filter to remove the element-coherent flow and extract the background-turbulence eddies. The filter intensity must be chosen carefully so that the background eddies are not eliminated or significantly distorted. Figures 7(a, e) showed that, for the filter applied throughout the paper, the filtered flow retained 97% of the total energy of the turbulent fluctuations $(u'^+)^2$ and $(v'^+)^2$. Here, we assess the sensitivity of the filtered $u'v'$ structures by comparing results based on filter levels that retain 100% (no filter), 99%, 97% and 95% of the fluctuating energy. The goal is to ensure that the location and topology of the background-turbulence structures remain consistent regardless of the filter intensity, while the element-coherent signal is effectively removed. As illustrated in figure 26, both the stem-scale wakes behind the elements in panel (a) and the shedding

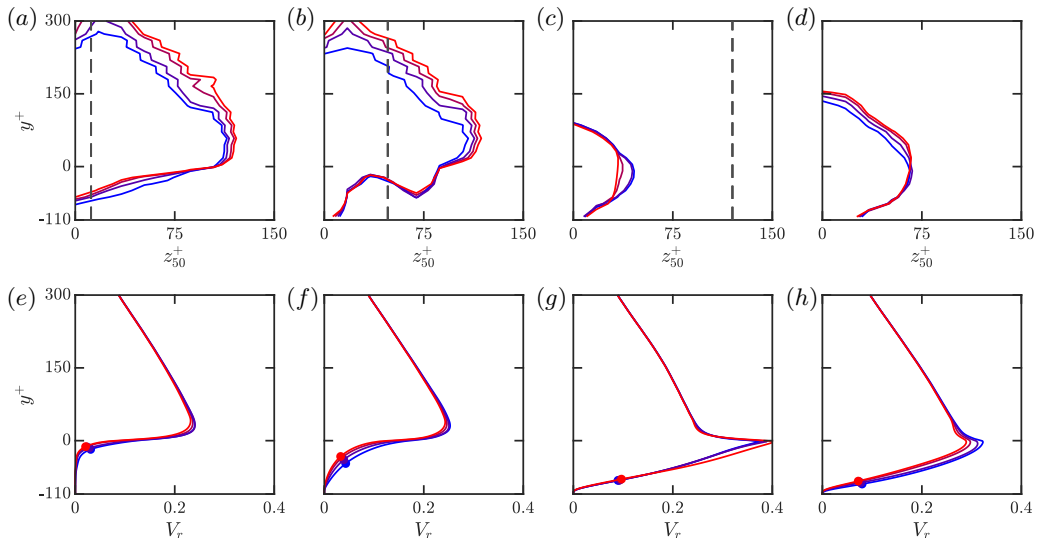


FIGURE 27. Characteristic spanwise width z_{50}^+ and relative volume V_r for canopies (a,e) $F_{S144 \times 36}$, (b,f) $I_{S72 \times 72}$, (c,g) $C_{S36 \times 144}$ and (d,h) $I_{S216 \times 216}$. From blue to red, the contours are based on filter levels at 100% (no filter), 99%, 97% and 95%. In (a-d), the contours enclose 75% of the penetrating eddies. The dashed lines mark the corresponding inter-element gap $g_z^+ \approx 12, 48, 120, 192$, respectively; markers \bullet indicate penetration depth where $V_r/V_{r,tip} = 0.25$. The dashed line is out of the boundary in (d).

eddies between the fences in panel (b) are effectively removed for filter levels $\leq 99\%$, while the background-turbulence structures remain mostly unaffected. This is consistent with the results shown in figures 27(a-d), where the characteristic width z_{50}^+ of eddies within the canopy remains similar across all filter levels. The collapse of the relative volume V_r and the penetration depth y_p^+ , shown in figures 27(e-h), further confirms that the applied filter essentially isolates the background turbulence without altering it significantly.

Appendix B. Sensitivity analysis for percolation threshold

In §3.1, we have performed a percolation analysis to ensure that $u'v'$ structures are separate from each other, by setting a threshold value for $u'v'$ to delimit the structures sufficiently high, while their volume is not unnecessarily shrunk by the threshold value being excessively high. Figure 8 shows that a percolation crisis occurs within the range $0.5 \lesssim H \lesssim 3$, and we selected a threshold at $H \approx 1.6$ to establish the size and location of the structures. Here, we assess the sensitivity of our results based on thresholds $H = 1.2, 1.6, 2.0$. As H decreases, new structures emerge while the existing ones expand in size, leading to a slight increase in the relative volume V_r at each height, as shown in figures 28(e-h). Nevertheless, the penetration depth y_p^+ remains consistent across all examined values of H . Similarly, figures 28(a-d) show that the characteristic spanwise width z_{50}^+ within and immediately above the canopies are similar for different H and only exhibit differences far above the canopy-tip plane. We can conclude that the influence of the choice of H in the range $H = 1.2$ -2 has no significant influence on our results and the ensuing conclusions.

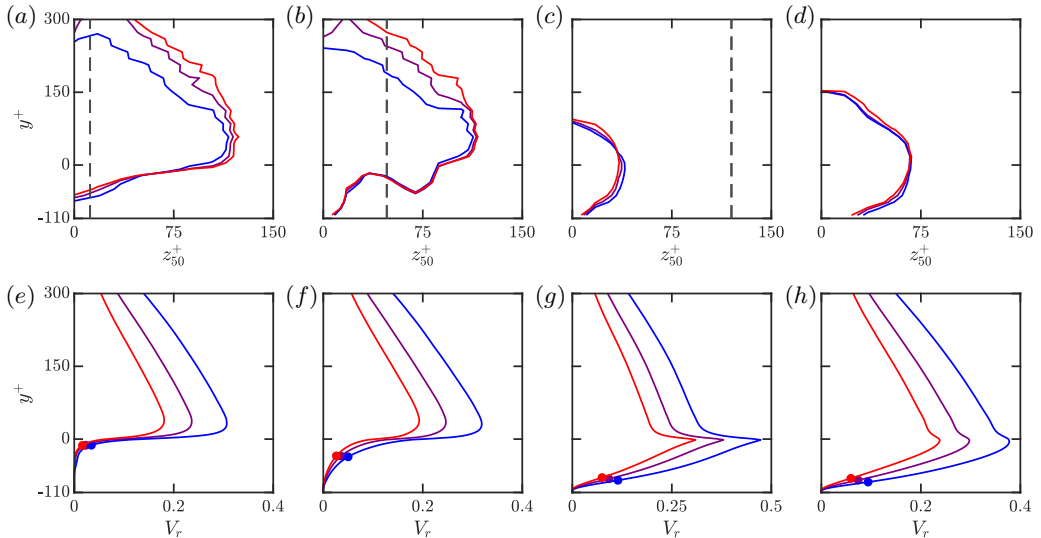


FIGURE 28. Characteristic spanwise width z_{50}^+ and relative volume V_r : canopies (a, e) $\text{FS}_{144 \times 36}$, (b, f) $\text{IS}_{72 \times 72}$, (c, g) $\text{CS}_{36 \times 144}$ and (d, h) $\text{IS}_{216 \times 216}$. From blue to red, the contours are based on thresholds $H = 1.2, 1.6, 2.0$, respectively. In (a-d), the contours enclose 75% of the penetrating eddies. The dashed lines mark the corresponding inter-element gap $g_z^+ \approx 12, 48, 120, 192$, respectively; markers • indicate penetration depth where $V_r/V_{r,\text{tip}} = 0.25$. The dashed line is out of the boundary in (d).

REFERENCES

- ABDERRAHAMAN-ELENA, N., FAIRHALL, C. T. & GARCÍA-MAYORAL, R. 2019 Modulation of near-wall turbulence in the transitionally rough regime. *J. Fluid Mech.* **865**, 1042–1071.
- AKBARI, H. & KOLOKOTSA, D. 2016 Three decades of urban heat islands and mitigation technologies research. *Energy Build.* **133**, 834–842.
- ARSHAD, A., ALI, H. M., ALI, M. & MANZOOR, S. 2017 Thermal performance of phase change material (pcm) based pin-finned heat sinks for electronics devices: Effect of pin thickness and pcm volume fraction. *Appl. Therm. Eng.* **112**, 143–155.
- BAILEY, B. N. & STOLL, R. 2013 Turbulence in sparse, organized vegetative canopies: a large-eddy simulation study. *Bound.-Layer Meteorol.* **147**, 369–400.
- BALDOCCHI, D. D. 2003 Assessing the eddy covariance technique for evaluating carbon dioxide exchange rates of ecosystems: past, present and future. *Glob. Change Biol.* **9** (4), 479–492.
- BELCHER, S. E. 2005 Mixing and transport in urban areas. *Phil. Trans. R. Soc. A* **363**, 2947–2968.
- BELCHER, S. E., HARMAN, I. N. & FINNIGAN, J. J. 2012 The wind in the willows: flows in forest canopies in complex terrain. *Annu. Rev. Fluid Mech.* **44**, 479–504.
- BERRY, P. M., STERLING, M., SPINK, J. H., BAKER, C. J., SYLVESTER-BRADLEY, R., MOONEY, S. J., TAMS, A. R. & ENNOS, A. R. 2004 Understanding and reducing lodging in cereals. *Adv. Agron.* **84** (04), 215–269.
- BLOCKEN, B. 2015 Computational fluid dynamics for urban physics: Importance, scales, possibilities, limitations and ten tips and tricks towards accurate and reliable simulations. *Build. Environ.* **91**, 219–245.
- BOGARD, D. G. & TIEDERMAN, W. G. 1986 Burst detection with single-point velocity measurements. *J. Fluid Mech.* **162**, 389–413.
- BREUGEM, W. P., BOERSMA, B. J. & UITTENBOGAARD, R. E. 2006 The influence of wall permeability on turbulent channel flow. *J. Fluid Mech.* **562**, 35–72.
- BRITTER, R. E. & HANNA, S. R. 2003 Flow and dispersion in urban areas. *Annu. Rev. Fluid Mech.* **35**, 469–496.

- BRUNET, Y. 2020 Turbulent flow in plant canopies: historical perspective and overview. *Bound.-Layer Meteorol.* **177**, 315–364.
- CAVA, D. & KATUL, G. G. 2008 Spectral short-circuiting and wake production within the canopy trunk space of an alpine hardwood forest. *Bound.-Layer Meteorol.* **126**, 415–431.
- CHAN, L., MACDONALD, M., CHUNG, D., HUTCHINS, N. & OOI, A. 2015 A systematic investigation of roughness height and wavelength in turbulent pipe flow in the transitionally rough regime. *J. Fluid Mech.* **771**, 743–777.
- CHEN, Z. & GARCÍA-MAYORAL, R. 2023 Examination of outer-layer similarity in wall turbulence over obstructing surfaces. *J. Fluid Mech.* **973**, A31.
- COLLINEAU, S. & BRUNET, Y. 1993 Detection of turbulent coherent motions in a forest canopy part ii: Time-scales and conditional averages. *Bound.-Layer Meteorol.* **66**, 49–73.
- CUI, J., PATEL, V. C. & LIN, C.-L. 2003 Large-eddy simulation of turbulent flow in a channel with rib roughness. *Int. J. Heat Fluid Flow* **24** (3), 372–388.
- DE LANGRE, E. 2008 Effects of wind on plants. *Annu. Rev. Fluid Mech.* **40**, 141–168.
- DEL ALAMO, J. C., JIMÉNEZ, J., ZANDONADE, P. & MOSER, R. D. 2006 Self-similar vortex clusters in the turbulent logarithmic region. *J. Fluid Mech.* **561**, 329–358.
- DUPONT, S., BONNEFOND, J.-M., IRVINE, M. R., LAMAUD, E. & BRUNET, Y. 2011 Long-distance edge effects in a pine forest with a deep and sparse trunk space: in situ and numerical experiments. *Agric. For. Meteorol.* **151** (3), 328–344.
- DUPONT, S., GOSSELIN, F., PY, C., DE LANGRE, E., HEMON, P. & BRUNET, Y. 2010 Modelling waving crops using large-eddy simulation: comparison with experiments and a linear stability analysis. *J. Fluid Mech.* **652**, 5–44.
- DUPONT, S. & PATTON, E. G. 2012 Influence of stability and seasonal canopy changes on micrometeorology within and above an orchard canopy: The chats experiment. *Agric. For. Meteorol.* **157**, 11–29.
- ESCOBEDO, F. J., KROEGER, T. & WAGNER, J. E. 2011 Urban forests and pollution mitigation: Analyzing ecosystem services and disservices. *Environ. Pollut.* **159** (8–9), 2078–2087.
- FINNIGAN, J. 2000 Turbulence in plant canopies. *Annu. Rev. Fluid Mech.* **32**, 519–571.
- FLORES, O. & JIMÉNEZ, J. 2010 Hierarchy of minimal flow units in the logarithmic layer. *Phys. Fluids* **22** (7), 071704.
- GARCÍA-MAYORAL, R. & JIMÉNEZ, J. 2011 Hydrodynamic stability and breakdown of the viscous regime over riblets. *J. Fluid Mech.* **678**, 317–347.
- GARDINER, B. A. 1994 Wind and wind forces in a plantation spruce forest. *Bound.-Layer Meteorol.* **67**, 161–186.
- HUANG, J., CASSIANI, M. & ALBERTSON, J. D. 2009 The effects of vegetation density on coherent turbulent structures within the canopy sublayer: a large-eddy simulation study. *Bound.-Layer Meteorol.* **133**, 253–275.
- JANHÄLL, S. 2015 Review on urban vegetation and particle air pollution–deposition and dispersion. *Atmos. Environ.* **105**, 130–137.
- JIMÉNEZ, J. 2012 Cascades in wall-bounded turbulence. *Annu. Rev. Fluid Mech.* **44**, 27–45.
- JIMÉNEZ, J. 2018 Coherent structures in wall-bounded turbulence. *J. Fluid Mech.* **842**, P1.
- JIMÉNEZ, J. 2013 Near-wall turbulence. *Phys. Fluids* **25** (10), 101302.
- JIMÉNEZ, J. & MOIN, P. 1991 The minimal flow unit in near-wall turbulence. *J. Fluid Mech.* **225**, 213–240.
- KAIMAL, J. C. & FINNIGAN, J. J. 1994 *Atmospheric boundary layer flows: their structure and measurement*. Oxford University Press.
- KIM, H., KLINE, S. J. & REYNOLDS, W. C. 1971 The production of turbulence near a smooth wall in a turbulent boundary layer. *J. Fluid Mech.* **50** (1), 133–160.
- KLINE, S. J., REYNOLDS, W. C., SCHRAUB, F. A. & RUNSTADLER, P. W. 1967 The structure of turbulent boundary layers. *J. Fluid Mech.* **30** (4), 741–773.
- LIGHTBODY, A. F. & NEPF, H. M. 2006 Prediction of velocity profiles and longitudinal dispersion in salt marsh vegetation. *Limnol. Oceanogr.* **51** (1), 218–228.
- LIGRANI, P. M., OLIVEIRA, M. M. & BLASKOVICH, T. 2003 Comparison of heat transfer augmentation techniques. *AIAA journal* **41** (3), 337–362.
- LOZANO-DURÁN, A., FLORES, O. & JIMÉNEZ, J. 2012 The three-dimensional structure of momentum transfer in turbulent channels. *J. Fluid Mech.* **694**, 100–130.

- LOZANO-DURÁN, A. & JIMÉNEZ, J. 2014 Time-resolved evolution of coherent structures in turbulent channels: characterization of eddies and cascades. *J. Fluid Mech.* **759**, 432–471.
- LOZANO-DURÁN, A. & JIMÉNEZ, J. 2014 Effect of the computational domain on direct simulations of turbulent channels up to $Re_\tau = 4200$. *Phys. Fluids* **26** (1), 011702.
- LU, S. S. & WILLMARTH, W. W. 1973 Measurements of the structure of the Reynolds stress in a turbulent boundary layer. *J. Fluid Mech.* **60** (3), 481–511.
- LUHAR, M., ROMINGER, J. & NEPF, H. 2008 Interaction between flow, transport and vegetation spatial structure. *Environ. Fluid Mech.* **8**, 423–439.
- MACDONALD, M., OOI, A., GARCÍA-MAYORAL, R., HUTCHINS, N. & CHUNG, D. 2018 Direct numerical simulation of high aspect ratio spanwise-aligned bars. *J. Fluid Mech.* **843**, 126–155.
- MALHI, Y. 2002 Carbon in the atmosphere and terrestrial biosphere in the 21st century. *Phil. Trans. R. Soc. A* **360**, 2925–2945.
- MARUSIC, I. & MONTY, J. P. 2019 Attached eddy model of wall turbulence. *Annu. Rev. Fluid Mech.* **51**, 49–74.
- MITTAL, R. & IACCARINO, G. 2005 Immersed boundary methods. *Annu. Rev. Fluid Mech.* **37**, 239–261.
- MONTI, A., OMIDYEGANEH, M., ECKHARDT, B. & PINELLI, A. 2020 On the genesis of different regimes in canopy flows: a numerical investigation. *J. Fluid Mech.* **891**, A9.
- MOUSA, M. H., MILJKOVIC, N. & NAWAZ, K. 2021 Review of heat transfer enhancement techniques for single phase flows. *Renew. Sustain. Energy Rev.* **137**, 110566.
- NAGAOSA, R. & HANDLER, R. A. 2003 Statistical analysis of coherent vortices near a free surface in a fully developed turbulence. *Phys. Fluids* **15** (2), 375–394.
- NARASIMHA, R., KUMAR, S. R., PRABHU, A. & KAILAS, S. V. 2007 Turbulent flux events in a nearly neutral atmospheric boundary layer. *Philos. Trans. R. Soc. A* **365**, 841–858.
- NEPF, H. M. 2012*a* Flow and transport in regions with aquatic vegetation. *Annu. Rev. Fluid Mech.* **44**, 123–142.
- NEPF, H. M. 2012*b* Hydrodynamics of vegetated channels. *J. Hydraul. Res.* **50** (3), 262–279.
- NOVAK, M. D., WARLAND, J. S., ORCHANSKY, A. L., KETLER, R. & GREEN, S. 2000 Wind tunnel and field measurements of turbulent flow in forests. part i: Uniformly thinned stands. *Bound.-Layer Meteorol.* **95**, 457–495.
- PELES, Y., KOŞAR, A., MISHRA, C., KUO, C.-J. & SCHNEIDER, B. 2005 Forced convective heat transfer across a pin fin micro heat sink. *Int. J. Heat Mass Transf.* **48** (17), 3615–3627.
- PIETRI, L., PETROFF, A., AMIELH, M. & ANSELMET, F. 2009 Turbulence characteristics within sparse and dense canopies. *Environ. Fluid Mech.* **9**, 297–320.
- POGGI, D., PORPORATO, A., RIDOLFI, L., ALBERTSON, J. D. & KATUL, G. G. 2004 The effect of vegetation density on canopy sub-layer turbulence. *Bound.-Layer Meteorol.* **111**, 565–587.
- RAHMAN, M. A., STRATOPOULOS, L. M. F., MOSER-REISCHL, A., ZÖLCH, T., HÄBERLE, K.-H., RÖTZER, T., PRETZSCH, H. & PAULEIT, S. 2020 Traits of trees for cooling urban heat islands: A meta-analysis. *Buill. Environ.* **170**, 106606.
- RAUPACH, MICHAEL R., FINNIGAN, JOHN J. & BRUNET, YVES 1996 Coherent eddies and turbulence in vegetation canopies: the mixing-layer analogy. *Bound.-Layer Meteorol. 25th Anniversary Volume, 1970–1995* pp. 351–382.
- REYNOLDS, W. C. & HUSSAIN, A. K. M. F. 1972 The mechanics of an organized wave in turbulent shear flow. part 3. theoretical models and comparisons with experiments. *J. Fluid Mech.* **54** (2), 263–288.
- SADIQUE, J., YANG, X. I. A., MENEVEAU, C. & MITTAL, R. 2017 Aerodynamic properties of rough surfaces with high aspect-ratio roughness elements: effect of aspect ratio and arrangements. *Bound.-Layer Meteorol.* **163**, 203–224.
- SHARMA, A. 2020 Turbulent flows over canopies. PhD thesis, University of Cambridge.
- SHARMA, A. & GARCÍA-MAYORAL, R. 2018 Turbulent flows over sparse canopies. *J. Phys. Conf. Ser.* **1001**, 012012.
- SHARMA, A. & GARCÍA-MAYORAL, R. 2020*a* Scaling and dynamics of turbulence over sparse canopies. *J. Fluid Mech.* **888**, A1.
- SHARMA, A. & GARCÍA-MAYORAL, R. 2020*b* Turbulent flows over dense filament canopies. *J. Fluid Mech.* **888**, A2.

- WALLACE, J. M., ECKELMANN, H. & BRODKEY, R. S. 1972 The wall region in turbulent shear flow. *J. Fluid Mech.* **54** (1), 39–48.
- WILLMARTH, W. W. & LU, S. S. 1972 Structure of the Reynolds stress near the wall. *J. Fluid Mech.* **55** (1), 65–92.
- WOODING, R. A., BRADLEY, E. F. & MARSHALL, J. K. 1973 Drag due to regular arrays of roughness elements of varying geometry. *Bound.-Layer Meteorol.* **5**, 285–308.
- YUE, W., MENEVEAU, C., PARLANGE, M. B., ZHU, W., HOUT, v. R. & KATZ, J. 2007 A comparative quadrant analysis of turbulence in a plant canopy. *Water Resour. Res.* **43** (5), W05422.